

AD-A168 814

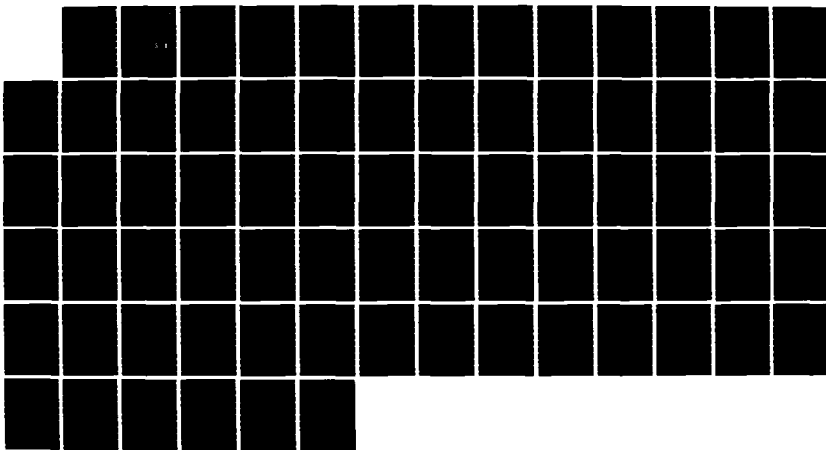
MODELING AND SIMULATION OF AN IMPLODING PLASMA  
RADIATION SOURCE(U) NAVAL RESEARCH LAB WASHINGTON DC  
S W MCDONALD ET AL. 85 JUN 86 NRL-MR-5785

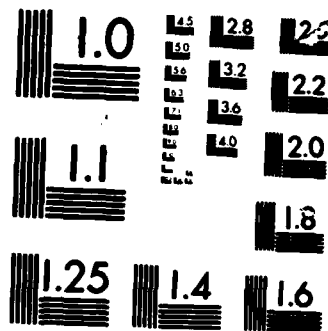
1/1

UNCLASSIFIED

F/G 20/14

NL





MICROCOPY

CHART

AD-A168 814

## Modeling and Simulation of an Imploding Plasma Radiation Source

S. W. McDONALD\* AND P. F. OTTINGER

*Plasma Technology Branch  
Plasma Physics Division*

*\*Laboratory for Plasma and Fusion Energy Studies  
University of Maryland  
College Park, MD 20742*

DTIC  
ELECTE  
JUN 20 1986  
S D

This work was sponsored by the Defense Nuclear Agency under Subtask T99QAXLA,  
work unit 00038 and work unit title "Plasma Erosion Switch Development."

DTIC FILE COPY

Approved for public release; distribution unlimited.

00 0 10 048

SECURITY CLASSIFICATION OF THIS PAGE

## REPORT DOCUMENTATION PAGE

1a. REPORT SECURITY CLASSIFICATION UNCLASSIFIED			1b. RESTRICTIVE MARKINGS		
2a. SECURITY CLASSIFICATION AUTHORITY			3. DISTRIBUTION/AVAILABILITY OF REPORT		
2b. DECLASSIFICATION/DOWNGRADING SCHEDULE			Approved for public release; distribution unlimited.		
4. PERFORMING ORGANIZATION REPORT NUMBER(S) NRL Memorandum Report 5785			5. MONITORING ORGANIZATION REPORT NUMBER(S)		
6a. NAME OF PERFORMING ORGANIZATION Naval Research Laboratory	6b. OFFICE SYMBOL (if applicable) Code 4770	7a. NAME OF MONITORING ORGANIZATION			
6c. ADDRESS (City, State, and ZIP Code) Washington, DC 20375-5000		7b. ADDRESS (City, State, and ZIP Code)			
8a. NAME OF FUNDING/SPONSORING ORGANIZATION Defense Nuclear Agency	8b. OFFICE SYMBOL (if applicable)	9. PROCUREMENT INSTRUMENT IDENTIFICATION NUMBER			
8c. ADDRESS (City, State, and ZIP Code) Washington, DC 20305		10. SOURCE OF FUNDING NUMBERS			
		PROGRAM ELEMENT NO. 62715H	PROJECT NO.	TASK NO.	WORK UNIT ACCESSION NO. DN320-094
11. TITLE (Include Security Classification) Modeling and Simulation of an Imploding Plasma Radiation Source					
12. PERSONAL AUTHOR(S) McDonald, S. W.* and Ottinger, P. F.					
13a. TYPE OF REPORT Interim	13b. TIME COVERED FROM TO	14. DATE OF REPORT (Year, Month, Day) 1986 June 5		15. PAGE COUNT 74	
16. SUPPLEMENTARY NOTATION *Laboratory for Plasma and Fusion Energy Studies, University of Maryland, College Park, MD 20742 (Continues)					
17. COSATI CODES			18. SUBJECT TERMS (Continue on reverse if necessary and identify by block number)		
FIELD	GROUP	SUB-GROUP	Imploding gas puff      Pulsed power generator		
			Plasma radiation source      Hot, dense plasma		
19. ABSTRACT (Continue on reverse if necessary and identify by block number) A simple theoretical model of a cylindrically imploding gas-puff plasma radiation source is described. This treatment, based on MHD single-fluid equations, includes models for the plasma equation of state, average ion charge level and temperature dependence of X-ray emission. Numerical results simulating the Naval Research Laboratory GAMBLE II pulsed-power device with an imploding plasma load are presented and compared with experiment. Parameter optimization results indicate that a reduction in the gas-puff nozzle radius from 1.25 cm to 0.9 cm could perhaps double the radiation yield.					
20. DISTRIBUTION/AVAILABILITY OF ABSTRACT <input checked="" type="checkbox"/> UNCLASSIFIED/UNLIMITED <input type="checkbox"/> SAME AS RPT. <input type="checkbox"/> DTIC USERS			21. ABSTRACT SECURITY CLASSIFICATION UNCLASSIFIED		
22a. NAME OF RESPONSIBLE INDIVIDUAL P. F. Ottinger			22b. TELEPHONE (Include Area Code) (202) 767-3066		22c. OFFICE SYMBOL Code 4771

DD FORM 1473, 84 MAR

83 APR edition may be used until exhausted.  
All other editions are obsolete.

SECURITY CLASSIFICATION OF THIS PAGE

**SECURITY CLASSIFICATION OF THIS PAGE**

**16. SUPPLEMENTARY NOTATION (Continued)**

This work was sponsored by the Defense Nuclear Agency under Subtask T99QAXLA, work unit 00038 and work unit title "Plasma Erosion Switch Development."

**SECURITY CLASSIFICATION OF THIS PAGE**

## CONTENTS

I. INTRODUCTION .....	1
II. DERIVATION OF EQUATIONS .....	2
III. THERMALIZATION OF KINETIC ENERGY .....	12
IV. ATOMIC PHYSICS: IONIZATION AND RADIATION .....	17
V. NUMERICAL RESULTS .....	23
VI. CONCLUSION .....	55
ACKNOWLEDGMENTS .....	55
APPENDIX A: CONSERVATION OF ENERGY .....	56
APPENDIX B: EQUATIONS OF MOTION .....	59
REFERENCES .....	66

Accession For	
NTIS CRA&I	<input checked="" type="checkbox"/>
DTIC TAB	<input type="checkbox"/>
Unannounced	<input type="checkbox"/>
Justification .....	
By .....	
Distribution /	
Availability Codes	
Dist	Avail and/or Special
A-1	



## MODELING AND SIMULATION OF AN IMPLODING PLASMA RADIATION SOURCE

### I. INTRODUCTION

The use of an imploding gas-puff plasma as a plasma radiation source (PRS) is of current experimental interest. In particular, a neon PRS has been used as a load for the GAMBLE II pulsed-power device at the Naval Research Laboratory, and has recently been measured<sup>1</sup> to produce approximately 2 kJ of kilovolt *K*-shell X-rays with a peak load current of 1.2 MA. In addition to the experimental applications, theoretical interest has grown concerning the plasma and atomic physics involved in the high-density ( $\sim 10^{19} \text{ cm}^{-3}$ ) pinch commonly achieved in these experiments: the plasma instabilities and radiation mechanisms are among the complicated processes which are still not completely understood. Between the experimental and theoretical research, there is a need for simple models of the physics of an imploding plasma with accompanying radiation that can be implemented in a tractable computer simulation of not only just the PRS itself, but of the entire pulsed-power device (generator, transmission line, switches, etc.) as well. As a primarily inductive load on the remainder of the circuit, the evolution of the PRS affects to some extent the behavior and efficiency of the entire system. Such a system simulation is important for investigating parameter regimes not currently available to the experiment in order to determine optimal design and operating parameters. As this type of simulation typically requires a large number of computer runs, in terms of speed and storage requirements the use of sophisticated one- or two-dimensional hydrodynamic models of the plasma coupled with complicated atomic physics algorithms is inappropriate. Thus, the intent of the model<sup>2,3</sup> contained in

Manuscript approved March 27, 1986.

the present report is to include just enough physics to adequately describe the evolution of the PRS (i.e., temperature-dependent effects such as radiation, ionization and "bouncing", etc.), yet computationally efficient in order to simulate the operation of the entire device.

In Section II, we will state our assumptions and derive the equations of motion which govern the imploding plasma. Section III discusses the details of the procedure used in the numerical implementation to convert part of the kinetic energy gained by the plasma during the run-in phase into thermal energy, ionization and radiation when the plasma collides on axis. The atomic physics model we use is described in Section IV. The implementation and use of the code *IMPLode* is detailed in Section V, along with numerical results compared with experimental observations (from *GAMBLE II*) and parameter optimization results. It will be shown in Appendix A that the ordinary differential equations evolved by the code conserve energy in that the power delivered to the PRS load by the external circuit is accounted for in various forms of stored energy and radiation; this is important from a design energy inventory point of view.

## II. DERIVATION OF EQUATIONS

The geometry of our model gas-puff plasma is that of a cylindrical annulus (Fig. 1) of length  $\ell$  with inner radius at  $r = b$  and outer radius at  $r = a$  inside a cylindrical cavity of wall radius  $r_w$ . The gas-puff is composed of a plasma with ion mass  $m_i = Am_p$  and mass/unit length  $\mu$ . The annulus itself is further divided into two concentric annular regions: an outer skin of skin depth  $\delta$  and a larger inner core. The boundary between the two regions is at a radius  $r = x$  (i.e.,  $x = a - \delta$ ). The current  $I$  in the plasma is assumed to flow only in the skin of conductivity  $\sigma$ , and the current density  $\underline{J} = J\hat{z}$  is assumed to be uniform,  $J = I/\pi(a^2 - x^2)$ . The two regions (core and skin) are allowed to have separate temperatures and are *not in thermal contact*; that is, there is no thermal diffusion between the regions. Quantities referring to the skin will be labelled with a subscript  $s$  and those of the core with



a subscript  $c$ : thus, the temperature and volume of the core and skin are respectively  $T_c, V_c$  and  $T_s, V_s$ .

We begin with the continuity equation

$$\frac{\partial \rho}{\partial t} + \underline{v} \cdot \nabla \rho = -\rho \nabla \cdot \underline{v}, \quad (1)$$

where  $\rho$  is the mass density,

$$\rho = n_i m_i + n_e m_e = n_i m_i + Z n_i m_e \equiv n m_i (1 + Z m_e / m_i) \approx n m_i = \frac{\mu}{\pi(a^2 - b^2)}, \quad (2)$$

and the number density  $n$  is defined as the ion density  $n_i$ . The first assumption will be

**A1.** The mass density (or ion density) is uniform over  $b < r < a$  (i.e., the same in both skin and core), but is allowed to vary in time.

Thus,

$$n(t) = \frac{\mu}{m_i \pi(a^2(t) - b^2(t))}. \quad (3)$$

Therefore, with  $\nabla n \equiv 0$ , (1) becomes an equation for the velocity profile  $v(r)$

$$\frac{\dot{n}}{n} = -2 \frac{a\dot{a} - b\dot{b}}{a^2 - b^2} = -\frac{1}{r} \frac{\partial}{\partial r} r v(r). \quad (4)$$

Now, the second assumption

**A2.** The inner radius moves with the same speed as the outer radius.

$$\dot{a} \equiv \dot{b} \equiv u. \quad (5)$$

With this, the equation for  $v(r)$  is

$$\frac{1}{r} \frac{\partial}{\partial r} r v(r) = \frac{2u}{a+b}, \quad (6)$$

which has the solution matching the boundary condition (5)

$$v(r) = \frac{abu}{a+b} \frac{1}{r} + \frac{u}{a-b} r \equiv \frac{A_1}{r} + A_2 r. \quad (7)$$

Note that this form for  $v(r)$  also holds as  $b \rightarrow 0$ , in which case  $A_1 \rightarrow 0$  so that  $v(r) = ur/a$  when the plasma annulus becomes a cylinder. There is a singularity here, however, in that the speed of the inner radius  $\dot{b} = v(b) = u$  does not smoothly go into  $v(0) = 0$  as  $b \rightarrow 0$ ; this will require special treatment later in the discussion of the implementation of these equations in the code and the concept of the "thermalization" procedure (see Section III). The velocity

profiles  $v(r)$  before and after  $b = 0$  are schematically depicted in Fig. 2. Assumptions A1 and A2 allow the continuity equation (1) to determine the velocity profile (7) in terms of the outer radius  $a$  and its velocity  $u$  (the inner radius  $b$  is given by  $b(t) = a(t) - w$ , where the width  $w$  of the annulus is constant:  $\dot{w} = \dot{a} - \dot{b} = 0$ ).

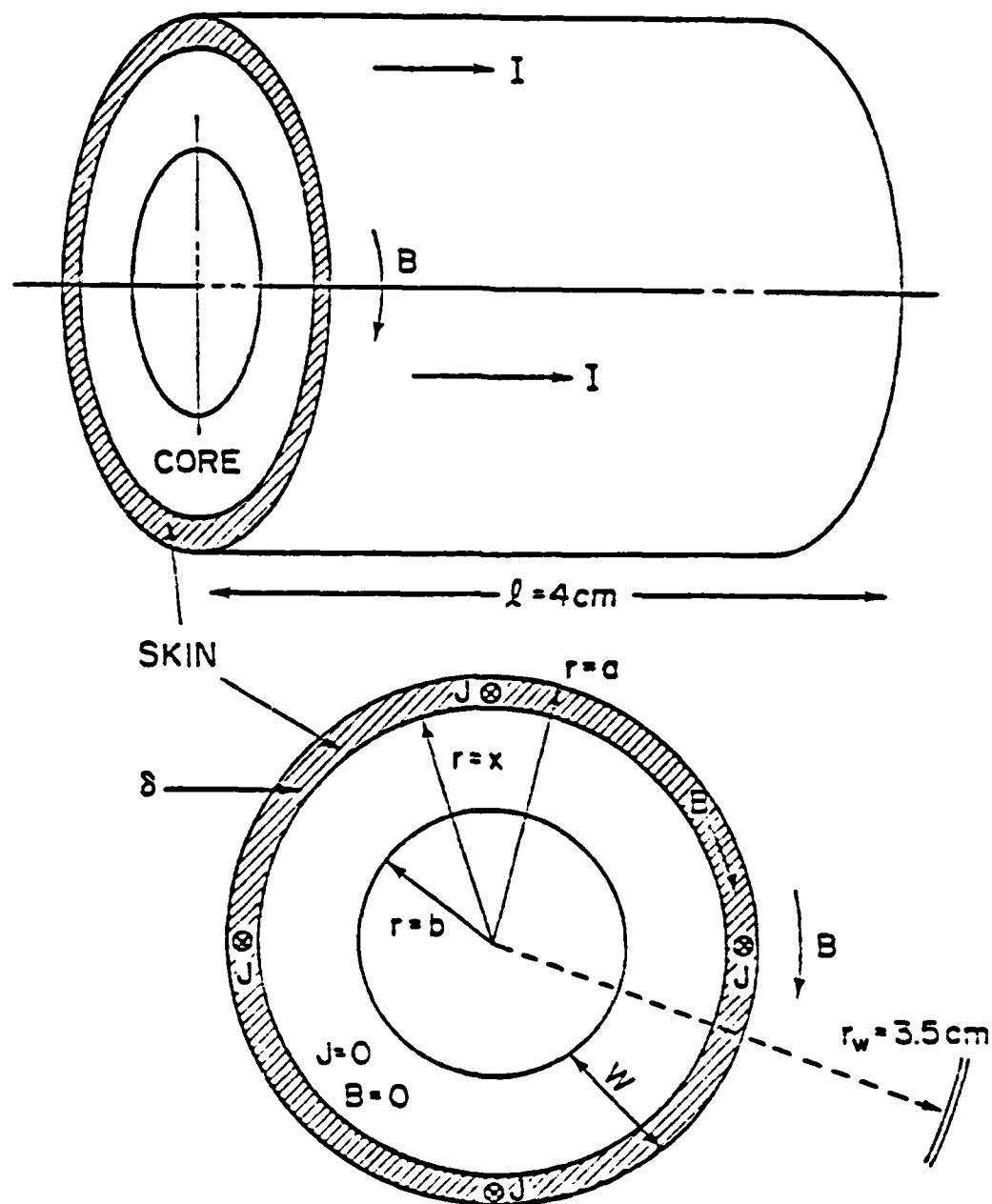


FIG. 1. Geometry of model gas-puff.

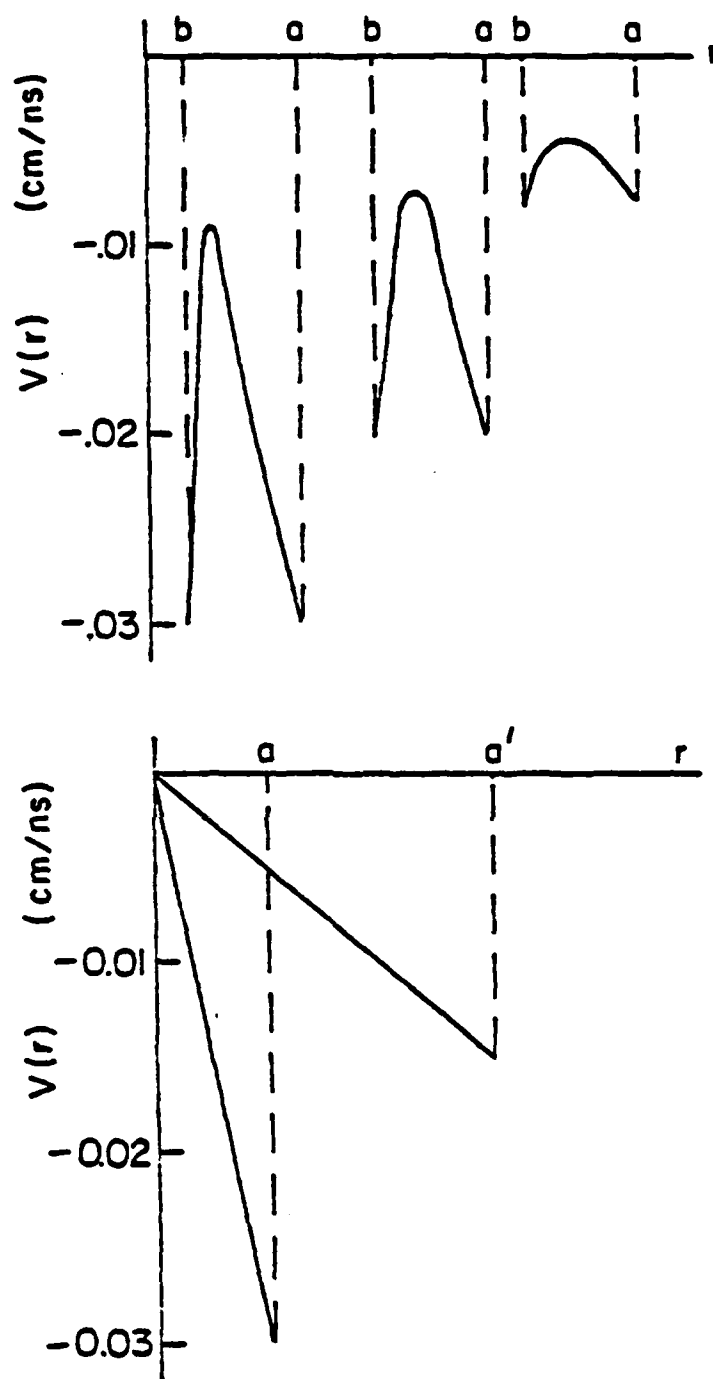


FIG. 2. Velocity profiles. (a)  $v(r)$  at three different times during the implosion phase as  $b \rightarrow 0$ , showing the steepening of the profile near  $r = b(t)$ . (b)  $v(r)$  after  $b = 0$  (pinch and post-pinch expansion phase).

Next, the force equation is used to derive an equation for the outer radius velocity  $u$ ,

$$\rho \left( \frac{\partial \underline{v}}{\partial t} + \underline{v} \cdot \nabla \underline{v} \right) = -\nabla p + \frac{1}{c} \underline{J} \times \underline{B}. \quad (8)$$

Since by assumption the current density is uniform over the cross section of the skin, the magnetic field  $\underline{B} = B(r)\hat{\theta}$  is easily computed to be

$$B(r) = \begin{cases} 0 & 0 < r < x \text{ (inner vacuum and core)} \\ \frac{2I}{cr} \frac{r^2 - x^2}{a^2 - x^2} & x < r < a \text{ (skin)} \\ \frac{2I}{cr} & a < r < r_w \text{ (vacuum)} \end{cases} \quad (9)$$

Now  $\rho$ ,  $v(r)$ ,  $J$ , and  $B(r)$  are all known quantities, so that the only unknown quantity in (8) is the pressure profile  $p(r)$ . Substitution of (2,7,9) into (8) would give a differential equation (in  $r$ ) for the pressure in terms of  $a(t)$ ,  $u(t)$  and  $\dot{u}(t)$ . However, the approach used by Guillory and Terry<sup>4</sup> is to integrate (8) over  $r$  so that the  $r$ -dependence of the equation is eliminated along with the  $\nabla p$  term (which would be evaluated at the endpoints,  $r = b$  and  $r = a$ ). This then gives an ordinary differential equation in time for the outer radius velocity  $\dot{u} = f(a, b, x, u, T)$ . This equation was used in an earlier version of the code (prior to March, 1985), and the problem with it seems to be that that procedure of integrating over  $r$  gives an equation which is inconsistent with energy conservation. This will not be discussed further here, but it will be shown (see Appendix A) that the present method does conserve energy (at least theoretically, and the code runs seem to bear this out).

In order to eliminate the  $r$ -dependence in (8) and derive an equation for  $\dot{u}(t)$ , first convert (8) into an equation for the kinetic energy density. Multiplying by  $\underline{v}$  one obtains

$$\rho \left( \frac{\partial}{\partial t} + \underline{v} \cdot \nabla \right) \frac{1}{2} v^2(r) = -\underline{v} \cdot \nabla p + \frac{1}{c} \underline{v} \cdot (\underline{J} \times \underline{B}). \quad (10)$$

Multiplying (1) by  $\frac{1}{2} v^2$  and adding the respective sides of that equation to (10), the evolution of the kinetic energy density  $\kappa \equiv \frac{1}{2} \rho v^2$  is found to satisfy

$$\frac{\partial \kappa}{\partial t} + \nabla \cdot (\kappa \underline{v}) = -\underline{v} \cdot \nabla p + \frac{1}{c} \underline{v} \cdot (\underline{J} \times \underline{B}). \quad (11)$$

Now integrating over the entire volume of the plasma, the total kinetic energy  $K(t)$  obeys

$$\dot{K}(t) = - \int dV \underline{v} \cdot \nabla p + \frac{1}{c} \int dV \underline{v} \cdot (\underline{J} \times \underline{B}). \quad (12)$$

The integral over the magnetic force term is only over the volume  $V_s$  of the skin. In obtaining the left-hand side of (12), the rule for time-varying volumes is used

$$\frac{d}{dt} \int_{V(t)} dV \kappa = \int_{V(t)} dV \frac{\partial \kappa}{\partial t} + \oint_{S(t)} d\hat{s} \cdot \underline{v}_S \kappa, \quad (13)$$

where  $\underline{v}_S$  is the local velocity of the surface bounding the volume. When (13) is used in the volume integral of (11), the term arising from  $\int dV \nabla \cdot (\kappa \underline{v}) = \oint d\hat{s} \cdot \underline{v} \kappa$  cancels the similar surface integral term in (13) if the local surface velocity  $\underline{v}_S$  is equal to the fluid velocity  $\underline{v}$  at that point on the surface. Here, of course, that is the case, and the conservative form of the left-hand side of (11,12) merely states that the kinetic energy of the plasma does not change due to particle flux through the bounding surfaces (at  $r = b$  and  $r = a$ ).

The pressure term in (12) can be converted to the following form

$$\begin{aligned} - \int dV \underline{v} \cdot \nabla p &= - \int dV \nabla \cdot (p \underline{v}) + \int dV p (\nabla \cdot \underline{v}) \\ &= - \oint_S d\hat{s} \cdot p \underline{v} + (\nabla \cdot \underline{v}) \int dV p \\ &= (\nabla \cdot \underline{v}) \left[ \int dV_c p + \int dV_s p \right] \\ &\equiv (\nabla \cdot \underline{v}) (V_c \bar{p}_c + V_s \bar{p}_s). \end{aligned} \quad (14)$$

In the second line, the fact that in this model the divergence of the velocity field is independent of position (6) allows it to be moved outside the integral. In the third line, the surface contribution of  $p \underline{v}$  vanishes because the pressure is assumed to vanish at  $r = a$  and either the pressure is zero at  $r = b$  (when  $b > 0$ ) or, when  $b = 0$ , the only bounding surface is at  $r = a$ . Also in the third line, the integral over the volume has been broken into the separate contributions from the core and the skin. Finally, in the fourth line, these separate contributions are expressed in terms of the average pressures of both regions,  $\bar{p}_c \equiv V_c^{-1} \int dV_c p$ , etc. The separate average temperatures and total number of particles (ions and electrons) in both regions are

$$V_{c,s} \bar{p}_{c,s} = V_{c,s} n(\bar{Z}_{c,s} + 1) \bar{T}_{c,s} = N_{c,s} \bar{T}_{c,s}, \quad (15)$$

where a third assumption is made:

**A3.** The ions and electrons in each region have the same temperature:  $\bar{T}_{c,s}^i = \bar{T}_{c,s}^e = \bar{T}_{c,s}$ .

Combining (12,14,15), the equation for the total kinetic energy is

$$\dot{K}(t) = \frac{2u}{a+b}(N_c \bar{T}_c + N_s \bar{T}_s) + (vJB). \quad (16)$$

Here, the formula for  $\nabla \cdot \underline{v}$  from (6) has been used, and the magnetic force term from (12) has been abbreviated by  $(vJB)$ . This is also the desired equation of motion for the outer radius velocity  $u(t)$ : substituting  $v(r)$  from (7) into the definition of the kinetic energy density, integrating over the total volume, then differentiating with respect to time and using this for the left-hand side of (16) produces an equation of the form

$$C_1 \dot{u} = -C_2 u^2 + C_{3c} \bar{T}_c + C_{3s} \bar{T}_s - C_4 I^2. \quad (17)$$

Since  $J$  and  $B(r)$  are also known, the  $(vJB)$  term can be evaluated to give the  $I^2$  term in (17). The coefficients  $C_i$  are functions of  $a, b, z, \bar{Z}_c, \bar{Z}_s$  and are explicitly given in Appendix B. This equation is coupled to the following temperature equations and should also be accompanied by a fourth first-order equation,  $\dot{a}(t) = u(t)$ .

The derivation of the equations governing the thermal energy or temperature in each region (skin and core) begins with the pressure equation found in Braginskii<sup>5</sup>

$$\frac{3}{2} \left[ \frac{\partial p}{\partial t} + \nabla \cdot (p\underline{v}) \right] = -p \nabla \cdot \underline{v} + \eta J^2 - R. \quad (18)$$

Here, the resistivity  $\eta$  is  $\sigma^{-1}$  and  $R$  is the radiated power density. From (8) recall that because the velocity and magnetic fields depend on  $r$ , so must the pressure (and in fact, (8) should probably be interpreted as an equation for the pressure profile). However, as in the case of the kinetic energy equation, we will integrate (18) over the volume in order to find an equation for the average pressures (or temperatures) of each region. Therefore, integrating (18) over the core and skin separately, one obtains

$$\frac{3}{2} \left[ \int dV_c \frac{\partial p}{\partial t} + \int dV_c \nabla \cdot (p\underline{v}) \right] = - \int dV_c p(\nabla \cdot \underline{v}) - \int dV_c R, \quad (19a)$$

$$\frac{3}{2} \left[ \int dV_s \frac{\partial p}{\partial t} + \int dV_s \nabla \cdot (p\underline{v}) \right] = - \int dV_s p(\nabla \cdot \underline{v}) - \int dV_s \eta J^2 - \int dV_s R. \quad (19b)$$

Now using the same rule for time-varying volumes as expressed in (13), these equations become

$$\frac{3}{2} \frac{d}{dt} \int dV_c p = - \int dV_c p(\nabla \cdot \underline{v}) - \int dV_c R \quad (20a)$$

$$\frac{3}{2} \frac{d}{dt} \int dV_s p = - \int dV_s p (\nabla \cdot \underline{v}) + \int dV_s \eta J^2 - \int dV_s R \quad (20b)$$

This step requires one important subtlety, however. In using the rule (13), one expects the surface integral term from (13) involving the local boundary velocity to cancel the surface integral arising from the divergence theorem applied to the  $\nabla \cdot (p\underline{v})$  term on the left-hand side of (19), which involves the local fluid velocity. Note that one of the surfaces involved in the surface integrals around both the skin and the core is the surface at  $r = x = a - \delta$ , the boundary between the skin and the core. For these surface integrals to cancel then, one must require that this boundary move with the local fluid velocity:  $\dot{x} = v(x)$ , where  $v(x)$  is the velocity profile (7) evaluated at  $r = x$ . This in turn implies that the skin depth must vary as  $\dot{\delta} = \dot{a} - \dot{x} = u - v(x)$ , as opposed to obeying any other phenomenological rule (such as  $\delta \sim (c/\omega_e)$ , or  $\delta = \text{constant}$ ). This is just a statement that thermal energy does not diffuse from one region to the other, as was originally assumed. Indeed, integrating the continuity equation (1) over the volumes of the skin and core separately, one finds that such a requirement on the motion of the boundary between them simply means that the total number of particles in each region remains constant:\* thus, thermal energy is not diffused by particles of the higher temperature in the skin moving into the lower temperature core region. If such diffusion were to be allowed, one would have to include other terms in the pressure equation (18). As it stands, however, this requirement on the variation of the skin depth is necessary for total energy conservation.

With (15), these equations can be converted into equations for the average temperatures of each region. In order to include the energy required for ionization, however, it is useful to introduce an alternate temperature which measures the total internal energy  $Q$  of the electron fluid. As defined by Terry and Guillory,<sup>6</sup> this is

$$Q \equiv T_e(Q) + \frac{2}{3} \frac{\Theta(Q)}{Z(Q)}, \quad (21)$$

---

\* Actually, this integration would show that the total number of ions in each region is constant; due to the provision in the model for ionization depending on temperature, the number of electrons in each region may vary.

where  $\Theta(Q)$  is the specific chemical potential, the energy required to ionize an atom to a charge  $Z$  while maintaining an ambient electron temperature  $T_e$ . When the quantities  $Q$  and  $Z$  are calculated properly in a collisional radiative equilibrium model, there will always be a one-to-one correspondence between  $Q$  and  $T_e$ . The inverse functions  $T(Q)$  and  $Z(T)$  then provide an equation of state, and only the time development of  $Q$  need be computed. Using (15), the spatially averaged pressures in (20a,b) can be recast in terms of the total internal energy of the fluid

$$\frac{3}{2}V_{c,s}\bar{p}_{c,s} \equiv U_{c,s} = \frac{3}{2}nV_{c,s}(\bar{Z}_{c,s}\bar{Q}_{c,s} + \bar{T}_{c,s}). \quad (22)$$

Since  $N_{c,s}^i = nV_{c,s}$  is time invariant and  $(\nabla \cdot \underline{v})$  is uniform in this model, the time development of  $Q_{c,s}$  is given by

$$\frac{3}{2}N_c \frac{d}{dt}(\bar{Z}_c\bar{Q}_c + \bar{T}_c) = -N_c(\bar{Z}_c + 1)\bar{T}_c(\bar{Q}_c)(\nabla \cdot \underline{v}) - V_c\bar{R}_c, \quad (23a)$$

$$\frac{3}{2}N_s \frac{d}{dt}(\bar{Z}_s\bar{Q}_s + \bar{T}_s) = -N_s(\bar{Z}_s + 1)\bar{T}_s(\bar{Q}_s)(\nabla \cdot \underline{v}) - V_s\eta J^2 - V_s\bar{R}_s. \quad (23b)$$

Here we have used  $\bar{p}V = N^i(\bar{Z} + 1)\bar{T}$  on the right-hand sides (instead of (22)) because only the internal energy of the *free* electron fluid contributes to the  $p dV$  work. This modification of Braginskii's heating relation involves only the partition of thermal energy: the source terms are undisturbed. Thus, the volume averaged radiated power density  $\bar{R}_{c,s}$  has been defined, and the fact that the current density  $J$  is uniform over the skin in this model has also been used.

The time derivative on the left-hand side of (23) becomes

$$\begin{aligned} \dot{U} &= \frac{3}{2}N^i(\dot{\bar{Z}}\bar{Q} + \bar{Z}\dot{\bar{Q}} + \dot{\bar{T}}), \\ &= \frac{3}{2}N^i(\bar{Z}'\bar{Q} + \bar{Z} + \bar{T}')\dot{\bar{Q}}, \end{aligned} \quad (24)$$

where  $\bar{Z}'$  and  $\bar{T}'$  are derivatives with respect to  $Q$ . In principle, this form for  $\dot{U}$  could be numerically implemented in the code, but instead the following expressions for  $\dot{U}$  and  $\dot{\bar{U}}$  have been used:

$$\begin{aligned} U_{c,s} &= \frac{3}{2}N_{c,s}^i(\bar{Z}_{c,s} + 1)\bar{Q}_{c,s} \\ \dot{U}_{c,s} &= \frac{3}{2}N_{c,s}^i(\bar{Z}_{c,s} + 1)\dot{\bar{Q}}_{c,s} \end{aligned} \quad (25)$$



This assumes

**A4.** *The energy of an ion is  $\frac{3}{2}\bar{Q}$  instead of  $\frac{3}{2}\bar{T}$ . This is merely a definition: for purposes of total energy inventory, as long as this definition is consistently used then it should not affect the conservation of energy.*

The expression for  $\dot{U}$  in (25) is a good approximation to the exact form (24) in the high temperature limit (where  $\bar{Z}' \approx 0$  and  $\bar{T}' \approx 1$ ). For this approximation we therefore assume

**A5.** *The rate of change of the charge state over a single timestep is negligible*

If assumption A5 is violated it could make a difference in determining if energy is conserved. If the charge state does change rapidly, one should use an iterative method to conserve energy at each timestep (such as that used in the thermalization step described in Section IV).

With (25) substituted for the left-hand sides of (23), the energy equations in the core and skin become

$$\dot{\bar{Q}}_c = -\frac{4}{3} \frac{u\bar{T}_c}{a+b} - \alpha_c \bar{R}_c, \quad (26a)$$

$$\dot{\bar{Q}}_s = -\frac{4}{3} \frac{u\bar{T}_s}{a+b} + \alpha_s \eta J^2 - \alpha_s \bar{R}_s. \quad (26b)$$

Here, we have inserted the definition of  $(\nabla \cdot \underline{v})$  from (6), and the coefficients  $\alpha$  are  $\alpha_{c,s} \equiv [\frac{3}{2}n(\bar{Z}_{c,s} + 1)]^{-1}$ . These equations close the set of ordinary differential equations. As stated earlier, they are to be solved in conjunction with rules for obtaining  $T(Q)$ ,  $Z(T)$  and the radiated power density  $R(T, n, Z)$ .

### III. THERMALIZATION OF KINETIC ENERGY

This Section discusses the procedure which is used in the code to convert some of the kinetic energy of the plasma at assembly time (when  $b \rightarrow 0$ ) into thermal energy. There are two reasons for making such a conversion:

- 1) In the real physical system, the kinetic energy gained during the implosion (or run-in) phase is partially converted into thermal energy as the various innermost components of the gas-puff "collide" on axis. The actual physical mechanism for this rapid heating probably involves collisional effects, counterstreaming plasma instabilities, possibly shock heating and other complicated processes. The theory contained in this report and implemented in the code, however, cannot (and does not intend to) treat these physical effects in any real way.
- 2) In the equations of motion derived in Section II and explicitly displayed in Appendix B, the velocity profile  $v(r)$  changes abruptly when  $b = 0$  (see Fig. 2): before  $b = 0$ , fluid elements at the inner radius  $b$  move inward with speed  $u = v(b) = v(a)$  (see Section II, assumption A.2) which, of course, becomes very large. After  $b = 0$ , however, the fluid velocity at  $r = b = 0$  is suddenly zero: the fluid elements approaching the axis are (artificially) abruptly stopped. Figure 3 shows a schematic picture of the kinetic energy profiles ( $\sim v^2(r)$ , from Fig. 2) before and after  $b = 0$ . Evidently, the total kinetic energy (the integral under these curves) contained in the plasma is greater when  $b \gtrsim 0$  than when  $b = 0$ , due to the abrupt change in velocity of the fluid elements near  $r = b \approx 0$ . This discrepancy in kinetic energy must be corrected for, or else the plasma will continue to evolve (with the new force equation coefficients valid for  $b = 0$ , Eqs.(B.10)) with less total energy than it had before the assembly time: this suggests the natural solution described below for converting this excess kinetic energy of fluid elements near the axis into thermal energy of the entire core.

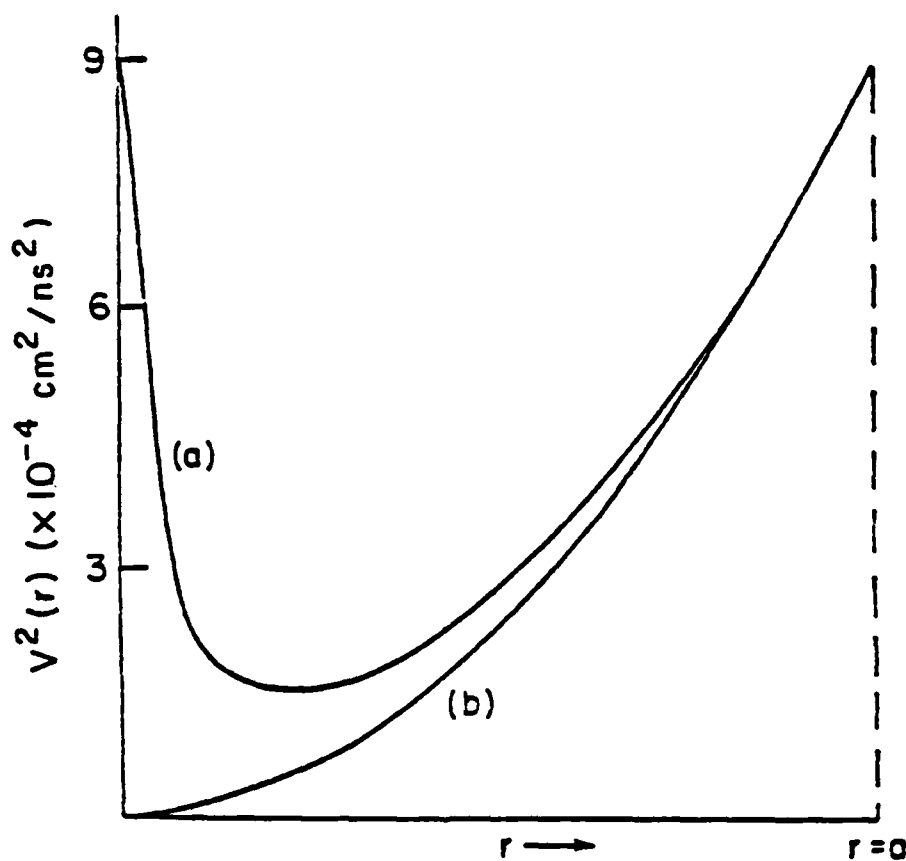


FIG. 3. Kinetic energy profiles ( $\sim v^2(r)$ ). (a) just before  $b = 0$ , showing large kinetic energy density near  $r = b$ . (b) just after  $b = 0$ , showing loss of kinetic energy near axis.

The conversion, or *thermalization* process used in the code proceeds as follows: assume that at the beginning of timestep  $n_a$  (time  $t_a = n_a \Delta t$ ), the inner radius  $b$  is for the first time less than some arbitrary small critical radius  $r_0$  (usually chosen to be 1mm). This is called the assembly time, or thermalization timestep, and this will be the step in which the equations of motion will be changed from those that hold before  $b = 0$  (Eqs.(B.14) with coefficients (B.9)) to those valid after  $b = 0$  (Eqs.(B.14) with (B.10)). Furthermore, after the calculations using the present value of  $b$  are finished,  $b$  will be set to zero.

The kinetic energy in the velocity profiles in Figs.(2,3) is computed in (B.3). The difference in this kinetic energy (to be thermalized) is simply

$$\Delta K = \frac{1}{4} \mu \ell u^2 \left[ \frac{2ab}{(a+b)^2} + \frac{4a^2 b^2 \ln(a/b)}{(a-b)(a+b)^3} \right]. \quad (27)$$

This energy is to be distributed over all the particles (ions and electrons) in the core as an increase in thermal energy  $\Delta Q$ :

$$\Delta K = \frac{3}{2} N_c \Delta Q = \frac{3}{2} (Z_c + 1) N_c^i \Delta Q. \quad (28)$$

Here,  $N_c^i = (\mu \ell / m_i) [(x^2 - b^2)/(a^2 - b^2)]$  is the number of ions in the core (a constant, see Section II), and  $N_c = (Z_c + 1) N_c^i$  is the total number of electrons and ions in the core at the beginning of this timestep. From (28), the new thermal energy per particle in the core after thermalization would be

$$Q_c^{(1)} = \Delta Q + Q_c^{(0)} = \frac{2\Delta K}{3(Z_c^{(0)} + 1)N_c^i} + Q_c^{(0)}. \quad (29)$$

Now,  $Q_c^{(0)}$  and  $Z_c^{(0)}$  are the values of the thermal energy per core particle and average core ion charge state at the beginning of the timestep. The problem with using  $Q_c^{(1)}$  for the new thermal energy in the rest of the timestep is that it is generally too large and will not conserve energy. To see this, consider the total amount of energy  $E_0$  available for thermal energy at the beginning of the timestep:

$$E_0 = \Delta K + \frac{3}{2} (Z_c^{(0)} + 1) N_c^i Q_c^{(0)}. \quad (30)$$

Using the equation of state (see Section IV), the new thermal energy per core particle  $Q_c^{(1)}$  would produce a core temperature  $T_c^{(1)}(Q_c^{(1)})$  and new ion charge state  $Z_c^{(1)}(T_c^{(1)})$  which

would be much greater than their values  $T_c^{(0)}$ ,  $Z_c^{(0)}$  at the beginning of the timestep. Thus, the new total core thermal energy  $U_c^{(1)}$  would be

$$\begin{aligned} U_c^{(1)} &= \frac{3}{2} N_c^i (Z_c^{(1)} + 1) Q_c^{(1)} \\ &= \frac{Z_c^{(1)} + 1}{Z_c^{(0)} + 1} \left[ \Delta K + \frac{3}{2} N_c^i (Z_c^{(0)} + 1) Q_c^{(0)} \right] \\ &= \frac{Z_c^{(1)} + 1}{Z_c^{(0)} + 1} E_0. \end{aligned} \quad (31)$$

For neon, the typical case is that  $Z_c^{(0)} \approx 1$ , while the initial thermalization estimate  $Q_c^{(1)}$  is enough to strip all but the innermost shell of electrons giving  $Z_c^{(1)} \approx 8$ . Therefore, if  $Q_c^{(1)}$  were used, the total core thermal energy  $U_c^{(1)}$  would be about 4-5 times the total amount of available energy  $E_0$  at the beginning of the timestep. Obviously, what has happened is that this energy  $E_0$  was not appropriately split into thermal and ionization energies.

The correct way to implement the thermalization would be to solve the implicit equation for  $Q_c^{(1)}$

$$\frac{3}{2} N_c^i \left[ Z_c^{(1)} (Q_c^{(1)} + 1) \right] Q_c^{(1)} = E_0, \quad (32)$$

using the equation of state (see Section IV). That is, one must adjust the new value of  $Q_c$  so that the corresponding number of electrons  $Z_c$  per ion have the self-consistent thermal energy  $Z_c Q_c$  to give a total core thermal energy  $U_c$  equal to the available energy  $E_0$ . Therefore, at the beginning of the thermalization timestep, the main routine *IMPLode* calls the subroutine *THERM*, which uses an iterative procedure to determine the new  $Q_c$ . This is described briefly below and illustrated in Fig. 4. Since  $Q_c^{(1)}$  is too large, a new trial value  $Q_c^{(2)}$  is taken to be the average of the initial value  $Q_c^{(0)}$  and  $Q_c^{(1)}$ . The total core thermal energy  $U_c^{(2)}$  is then computed with the new charge state  $Z_c^{(2)}$  and compared with the constant value  $E_0$ . If  $U_c^{(2)}$  is still greater than  $E_0$ ,  $Q_c^{(3)}$  is chosen as an average between  $Q_c^{(0)}$  and  $Q_c^{(2)}$ ; if  $U_c^{(2)} < E_0$ ,  $Q_c^{(3)}$  is taken to be the average of  $Q_c^{(1)}$  (too high) and  $Q_c^{(2)}$ . This method of "splitting the difference" continues until the values of  $U_c^{(n)}$  and  $E_0$  agree to within some tolerance (usually picked to be about 10%).

$$E_0 = \Delta K + \frac{3}{2}(Z_c^{(0)} + 1)N_c^i Q_c^{(0)}$$

$$Q_c^{(1)} = \Delta Q + Q_c^{(0)} = \frac{2\Delta K}{3(Z_c^{(0)} + 1)N_c^i} + Q_c^{(0)}$$

$$Q_{min} = Q_c^{(0)}$$

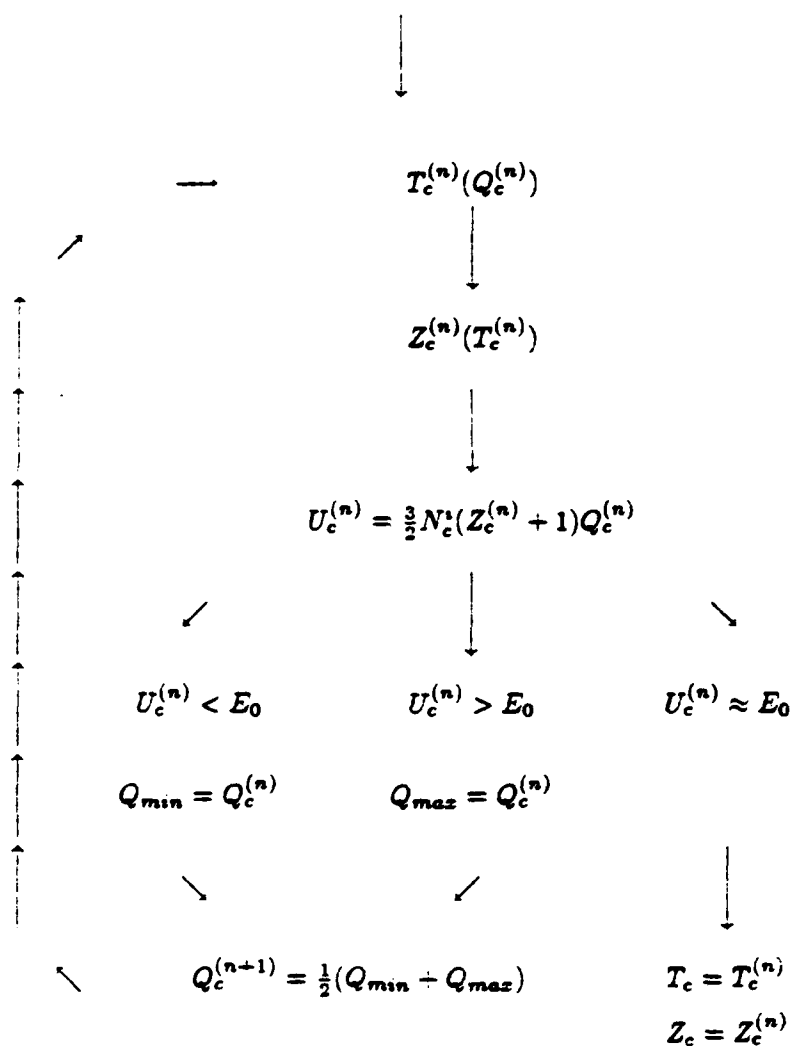


FIG. 4. Flowchart illustrating thermalization procedure used in subroutine THERM.

As an example of the numbers involved, in a particular code run the core plasma had the following parameters at the beginning of the thermalization timestep:  $N_e^i \approx 3.5 \times 10^{18}$ ,  $Q_e^{(0)} = 20.1 \text{ eV}$ ,  $T_e^{(0)} = 4.5 \text{ eV}$ ,  $Z_e^{(0)} = 1.38$ . With a kinetic energy  $\Delta K = 1795 \text{ J}$  to be thermalized, these produce the initial values  $\Delta Q = 884 \text{ eV}$ ,  $U_e^{(0)} = 40.1 \text{ J}$ , and  $E_0 = 1835 \text{ J}$ . After  $n = 10$  iterations, the final thermalized values were determined to be  $Q_e^{(n)} = 273 \text{ eV}$ ,  $T_e^{(n)} = 158 \text{ eV}$ ,  $Z_e^{(n)} = 8.0$ , and  $U_e^{(n)} = 1833 \text{ J}$ .

#### IV ATOMIC PHYSICS: IONIZATION AND RADIATION

The reason for developing this model of an imploding plasma radiation source is to be able to compute the amount of radiation produced by the plasma. The description of the atomic physics involved in collisional ionization and radiation can be on many different levels and can be based on several different models. The primary concern, however, is to keep this simulation as simple as possible so that it can be used in conjunction with a simulation of the entire pulsed-power device for purposes of design and operating parameter optimization. Thus, for purposes of determining ionization levels and radiation we have used the results of Terry and Guillory;<sup>6</sup> these are in the form of piecewise numerically-fit curves giving an equation of state, and average ion charge state and radiated power density as functions of plasma electron temperature and density for neon and argon. The original data for the equation of state and radiated power density were obtained from collisional radiative equilibrium calculations due to D. Duston.

##### A. EQUATION OF STATE and AVERAGE ION CHARGE STATE

An equation of state is used to determine the branching of "thermal energy" per electron  $\frac{3}{2}Q$  into actual thermal energy  $\frac{3}{2}T$  and the energy  $\Theta$  needed to ionize the average atom to a charge state consistent with the electron temperature  $T$ . As in equation (21), this quantity  $Q$  has been defined as

$$\frac{3}{2}Z(T)Q \equiv \frac{3}{2}Z(T)T(Q) + \Theta(T), \quad (33)$$

where  $\Theta(T(Q))$  is the energy required to ionize an atom to an average charge state of  $Z(T(Q))$ . When  $Q$  is incremented at each timestep, the subroutine *TFUNC* is called to determine  $T(Q)$  and subroutine *ZFUNC* is then called to determine  $Z(T)$ . These values of  $T$  and  $Z$  are used in computing the coefficients in the differential equations for the next timestep. For neon, a numerical fit<sup>6</sup> for the branching ratio  $B(Q)$  is used where

$$B(Q) \equiv \frac{Q}{T(Q)} = 1 + \frac{2\Theta(Q)}{3Z(Q)T(Q)}. \quad (34)$$

Thus, knowing  $Q$ , *TFUNC* simply computes  $B(Q)$  and hence  $T(Q) = Q/B(Q)$ . (Actually, the piecewise fit in *TFUNC* is based on the logarithms of  $Q$  and  $B$ .) The graph of  $\ln T$  as a function of  $\ln Q$  for neon is shown in Fig. 5. Subroutine *ZFUNC* uses a numerical piecewise-linear fit<sup>6</sup> to a curve  $Z(T)$ , as shown in Fig. 6. The code is also capable of treating an argon plasma, but results will only be presented for neon.

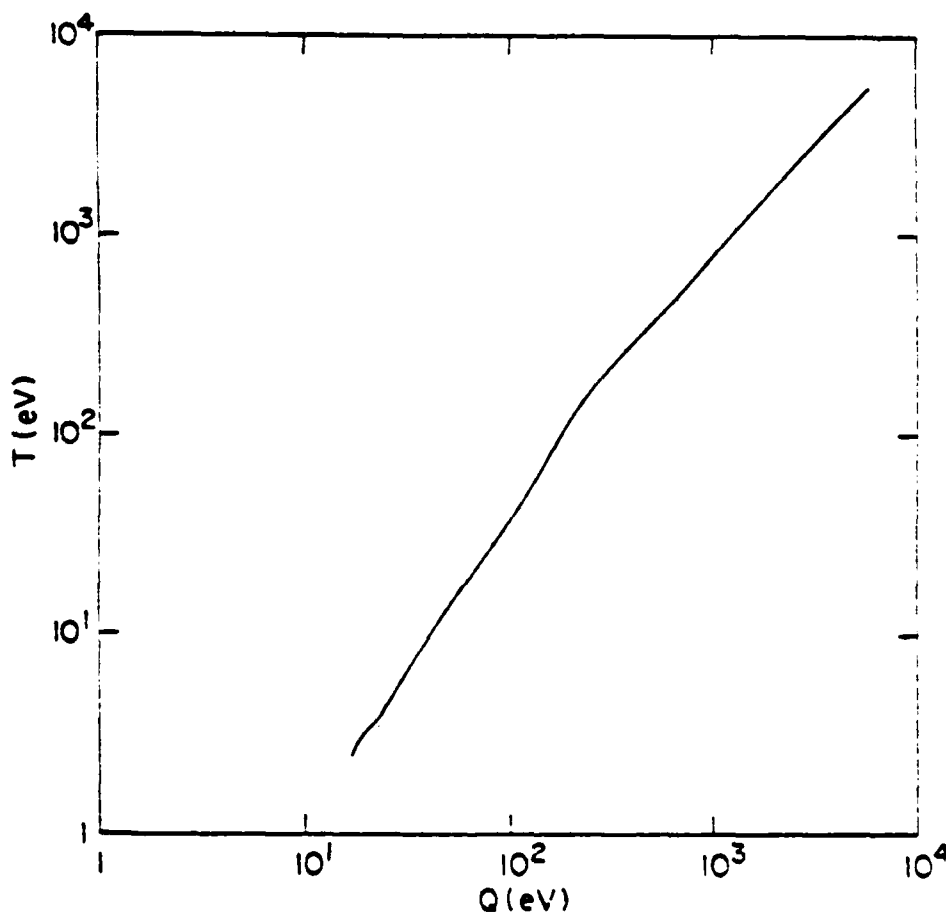


FIG. 5. Equation of state for neon,  $T(Q)$ . Supplied by R. E. Terry.



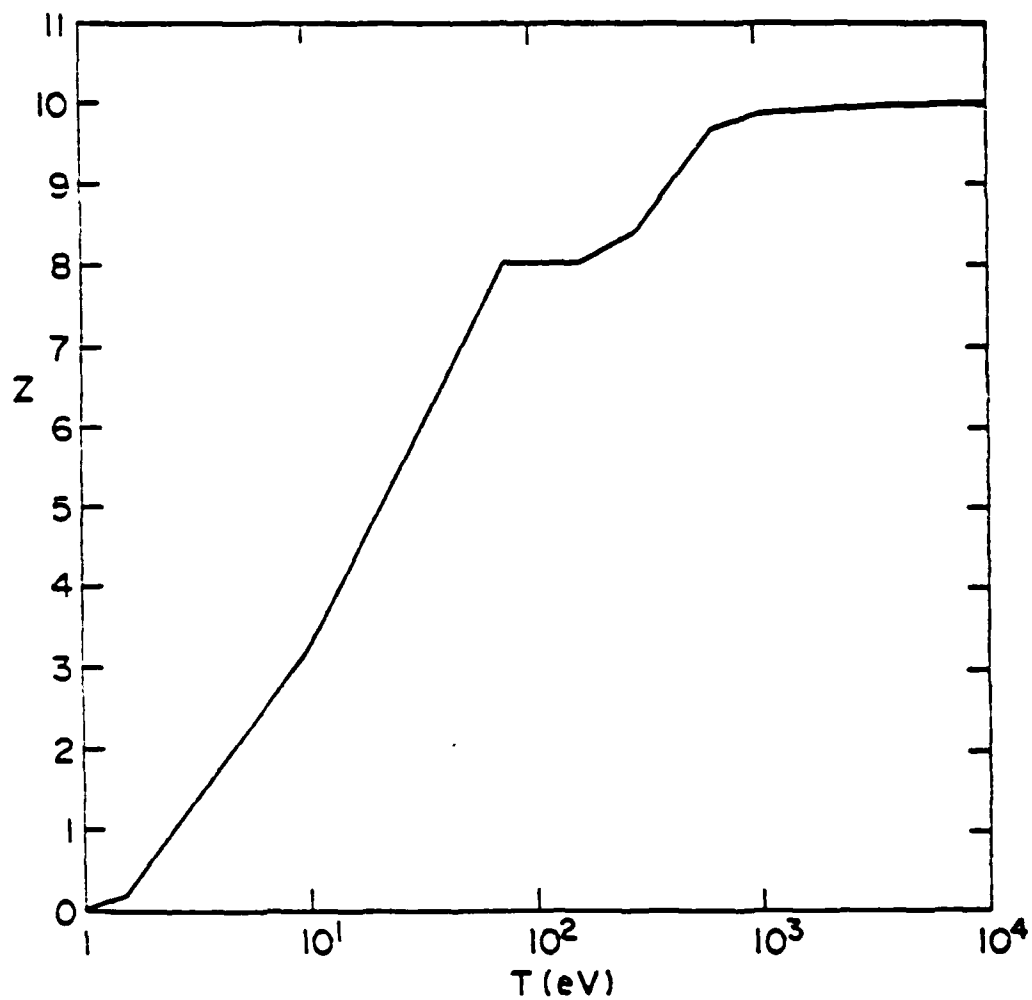


FIG. 6. Average ion charge state for neon,  $Z(T)$ . Supplied by R. E. Terry.

## B. RADIATED POWER DENSITY

In order to compute the radiated power density from the imploding plasma, we have used the results of more sophisticated atomic physics computer calculations produced by Terry.<sup>6</sup> These are in the form of piecewise-spline fitted numerical tables for continuum and line radiation as a function of electron temperature and ion density. Four types of radiation are considered: Bremsstrahlung, free-bound, and *K*-shell and *L*-shell *X*-rays. The radiated power density ( $\text{W}/\text{cm}^3$ ) curves for these types of radiation for neon at an ion density of  $n_i = 10^{18}$  are shown in Fig. 7. Of particular experimental interest are the *K*-shell emission in neon and the *L*-shell line in argon: these Figures show that both of these lines peak at about 400 eV for the respective elements. Each type of radiation is produced with a power density that scales roughly as the square of the ion density. These curves are the result of the subroutine *CREMIT* obtained from R. E. Terry.<sup>6</sup>

The comparison of numerically computed radiation yields with those observed in experiments are based on several aspects of the radiation pulse: total amount of radiated energy ( $Y_T$ , including all types of radiation), total radiated *K*-shell and *L*-shell *X*-ray energy ( $Y_K$  and  $Y_L$ ), *X*-ray efficiency (ratio of  $Y_K$  or  $Y_L$  to  $Y_T$ ) and the length of the radiation pulse. We have found that on a typical code run with plasma parameters which can be matched with a corresponding experiment, the radiation yields  $Y_T$  and  $Y_K$  or  $Y_L$  do not agree with the experimentally observed values. However, as the plasma parameters are varied in both the numerical simulations and the experiment, the behavior of the numerically computed yields appears to follow that of the experiment. For example, fixing the initial plasma radius (or nozzle radius) and generator voltage, the radiated yields increase to a maximum and then decrease again as the mass per unit length  $\mu$  is varied: this is observed in both simulation and experiment, although the magnitudes of the yields do not agree (the simulation values are generally greater).

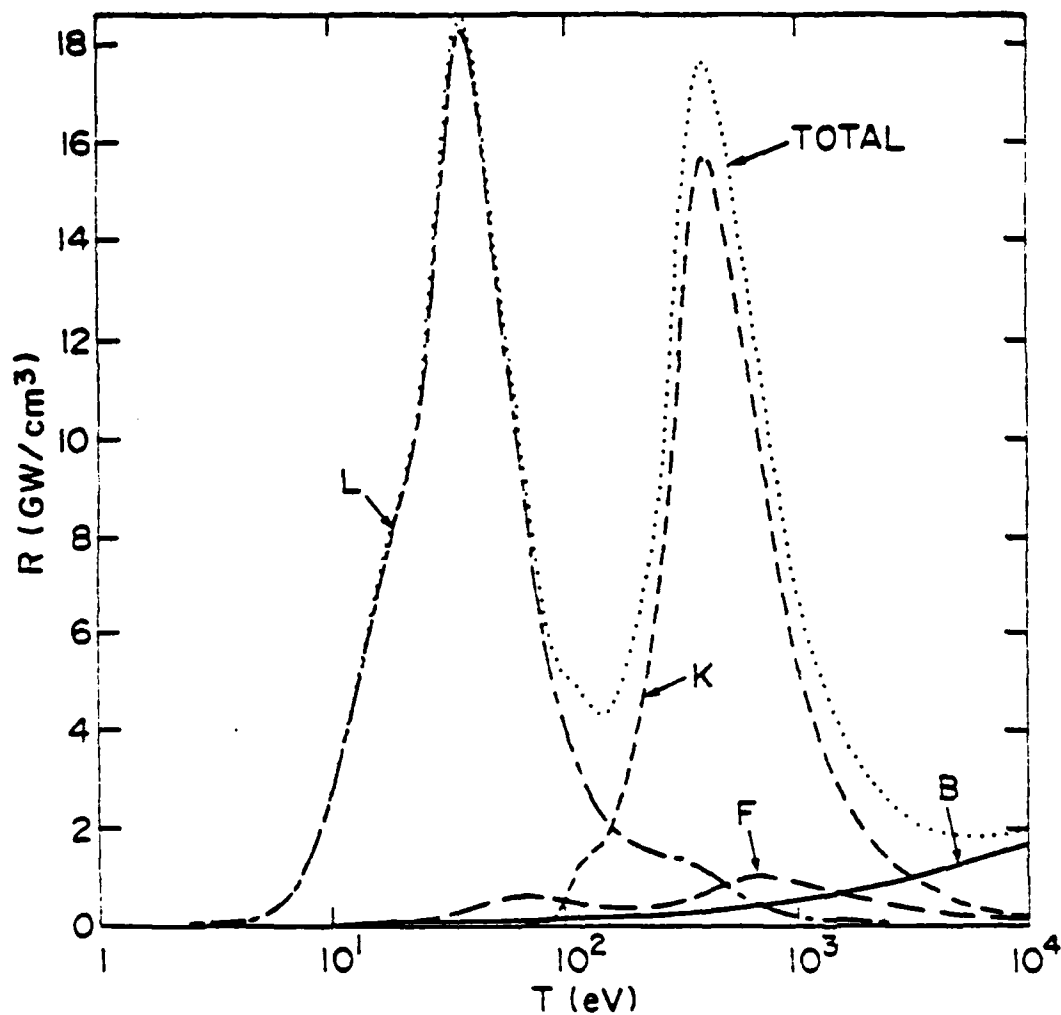


FIG. 7. Radiated power density for neon as a function of electron temperature at an ion density of  $n_i = 10^{18} \text{ cm}^{-3}$ . Four types of radiation are shown: *L*-shell (*L*) and *K*-shell (*K*) X-rays, Bremsstrahlung (*B*) and Free-bound (*F*) continuum radiation. The total radiated power density is represented by the dotted curve. Obtained from R. E. Terry.

Because of this similar behavior, we have attempted to bring the computed yields into better agreement with the experimentally measured values by introducing an overall radiation multiplicative factor called the *opacity*. The way in which this artificial factor is set (usually a number between zero and one) is described in the next Section; once chosen however, (at a particular set of parameter values) it is found that the simulations are in much better agreement with experiment over a wide range of parameter values. The implementation of this factor is simple: at each timestep, the radiated power densities  $R_e$  and  $R_i$  must be computed not only for contributing to the total radiated energy, but also for acting as an energy sink in the evolution equations (26) for  $Q_e$  and  $Q_i$ . Thus, the main routine *IMPLode* calls the subroutine *PLOSS*, which in turn calls *CREMIT*. When *CREMIT* returns the values of the four types of radiated power densities for the current temperature and plasma density, *PLOSS* simply multiplies each by the value of the opacity factor and returns the results to *IMPLode* for use in the evolution equations and radiated energy compilation. Note that while the use of the opacity factor usually means that less total energy is radiated, it also means that the radiation is less of a sink for the thermal energy  $Q$ . This tends to keep the temperature of the plasma up, but actually this is a complicated effect: not only is the radiation a temperature dependent quantity, but as the temperature remains high, so does the plasma pressure during the pinch phase so that the minimum radius achieved is greater (lower pinch density), again reducing the radiation.

As will be seen in the next Section on numerical results, the peak core temperature typically observed at pinch time (time of minimum radius or maximum density) is around 400-500 eV, compared with experimentally measured values of about 100-200 eV. The total radiations yields, however, agree well with the experiment (with the use of the opacity factor). This is somewhat of a contradiction, because for maximum  $K$ -shell yield (in neon), the radiation curves in Fig. 7 indicate that at pinch the temperature should be precisely in this range, yet the experiments suggest that the optimum temperature for  $Y_K$  should be nearer 100 eV. Thus, not only should the temperatures in the simulation remain lower,

but there should be a corresponding shift in the radiation curves to lower temperatures (otherwise, very little radiation would be computed). One possibility is that the equations of state that are used are not appropriate: that is, it may take much more energy than  $\Theta = \frac{3}{2}Z(Q - T)$  given by our equations of state to ionize an atom to the average value  $Z$ . Correcting for this would mean dumping more available "thermal energy"  $Q$  into ionization energy than presently used: this would act to keep the temperature down. The effect of true plasma opacity to  $L$ -shell radiation at lower temperatures (in neon) on the  $K$ -shell yield has also been suggested<sup>7</sup> as a phenomenon not accounted for in the radiation curves which could possibly lower the optimum  $K$ -shell radiation temperature (in neon) to the 100-200 eV level.

## V. NUMERICAL RESULTS

This Section discusses the use of the code *IMPLode* for comparison with experiment and parameter optimization, and then we discuss some of the numerical results. First, the input parameters available to the user which set the properties of gas-puff and its environment and which remain constant through a single code run are

Parameter	Computer Variable	Definition	Units	Typical Value
$a_0$	a0	initial radius	cm	1.25 cm
$\mu$	dm	mass/length	g/cm	$3.0 \times 10^{-5}$ g/cm
$\ell$	xl	length	cm	4.0 cm
$w$	w	annulus width	cm	0.3 cm
$A$	aion	atomic weight	1	20.183
opacity	opac	opacity	1	0.25
$\delta_0$	delt0	initial skin depth	cm	0.1 cm
$r_0$	r0	critical radius	cm	0.1 cm
$r_w$	rw	wall radius	cm	3.5 cm
$V_G$	vpeak	generator voltage	MV	3.0 MV
$v_0$	v0	initial velocity	cm/ns	0.0

The values given are for a typical code run with neon in the *GAMBLE II* configuration of Fig. 8 near optimum mass/length at an open circuit generator voltage of 3MV (peak load current  $\sim 1.2\text{MA}$ ). All of these input parameters are local to *IMPLode* and its accompanying subroutines, except for  $V_G$  which is actually input with the system configuration parameters (the remainder of which, such as line inductances, are not listed here). The value of the atomic weight  $A$  should be either 20.183 (neon) or 40.0 (argon). In principle, other species can be used; presently, however, models exist in the code for only neon and argon. The initial skin depth  $\delta_0$  is of course not an input parameter in the version of the code which does not have a skin (see Appendix B). The critical radius  $r_0$  is that which the inner radius  $b$  of the gas-puff must reach for the thermalization step to occur. The parameters of most interest for design optimization are  $a_0$ ,  $\mu$  and  $V_G$ . Those which should be varied to analyze the behavior of the model itself are  $w$ , *opacity*,  $\delta_0$  and  $r_0$ . The parameters  $\ell$ ,  $r_w$  and  $A$  depend on the experimental situation, and  $v_0$  is generally always taken to be zero.

#### A. SETTING PARAMETERS TO COMPARE WITH EXPERIMENT

In order to predict optimal performance from numerical simulations, one must first check whether the code results agree with present experimental observations, and make necessary adjustments if they do not. The first step in setting the code parameters to coincide with experimental parameters is to choose the correct system configuration in the transmission line code<sup>8</sup> (TLC), including the value of the peak generator open circuit voltage  $V_G$ . The comparison with experiment is best made in terms of the profile of the current flowing in the load (the PRS): the primary points of comparison are the peak load current  $I_P$  and the time  $t_P$  at which the peak occurs relative to the generator discharge. This comparison can be made with almost any reasonable values of the other parameters (although one should try to get an estimate of the appropriate values from the experiment), as  $I_P$  is fairly insensitive to the other parameters (a slight variation in  $I_P$  with  $\mu$  at fixed  $V_G$  has been observed).

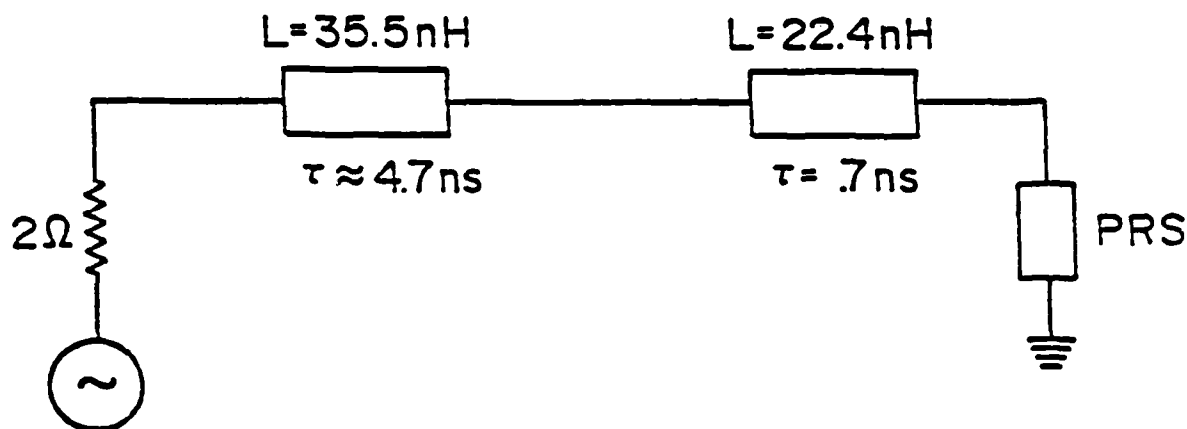


FIG. 8. Transmission line configuration for *GAMBLE II* experiment used in simulation.

The parameters  $a_0$  and  $\mu$  are fairly difficult to determine from a particular experimental run. Streak photographs of visible light and X-rays from the implosion and data from the nozzle manufacturer show that the gas-puff is not axially uniform: it tends to expand radially as it moves away from the nozzle, so that  $a_0$  and  $w$  appear to increase along the axial direction. Furthermore, the initial plasma density profile is not uniform in the radial direction across the annular region. These effects make it difficult to define what the appropriate "outer radius" and thickness  $w$  should be for the model. The experimental measure of the mass per unit length  $\mu$  of the gas is in terms of the initial plenum pressure. It is believed that over the parameter range studied this plenum pressure should be linearly related to  $\mu$ , but there is not an *a priori* model for this relationship. Moreover, one-dimensional simulations which include the effects of anomalous resistivity<sup>9</sup> in the early phase of the implosion suggest that some mass is left behind as the load is snowplowed up.

It will be shown below that at fixed  $a_0$  and  $V_G$  there is an optimum value of  $\mu$  in the simulation and an optimum plenum pressure in the experiment. Having matched  $a_0$  and  $V_G$  to the experiment, one can identify the optimum value of  $\mu$  with the optimum plenum pressure. This value of  $\mu$  must be interpreted carefully: it may measure only the mass remaining in front of the magnetic piston after the early resistive field penetration has ceased. Whatever the real meaning, keeping the nozzle radius  $a_0$  constant, the optimal

values of  $\mu$  and plenum pressure can be compared for different values of the peak current  $I_P$  (or  $V_G$ ) to determine a fairly linear relationship.

## B. SETTING THE OPACITY

In order to scale the radiation yield produced in the simulation (i.e., determine the *opacity*), the following procedure is used. Matching  $a_0$  and  $I_P$  (or  $V_G$ ) to experimental values, the *opacity* is set to unity and  $\mu$  is varied to compute radiation yields  $Y_T$ ,  $Y_K$  and  $Y_L$  as a function of  $\mu$ . At the value of  $\mu$  at which  $Y_K$  is maximum for neon ( $Y_L$  for argon), we compare  $Y_K$  ( $Y_L$ ) with the experimental value. As stated in Section IV, the radiation yields computed in the simulation with unit opacity will generally be higher than that measured in experiment. Thus, one proceeds to reduce the opacity and compute the radiation yields at fixed  $a_0$  and  $V_G$ , keeping  $\mu$  set at the optimum value. Once a value of the opacity is found that produces yields that are in good agreement with experiment, the mass/length is again varied (at this new opacity) in the neighborhood of the optimum  $\mu$ : this is because the optimum  $\mu$  is generally shifted slightly higher as the opacity is reduced. This procedure can be repeated until the desired agreement with experiment is reached for some combination of opacity at optimum  $\mu$ . For neon, with nozzle radius  $a_0 = 1.25$  cm and  $V_G = 3.0$  MV ( $I_P = 1.2$  MA), the optimum mass/length was found to be  $\mu = 30$   $\mu\text{g}/\text{cm}$  with an opacity of 0.25. In the version of the code without the skin (see Appendix B), the optimum mass was 38  $\mu\text{g}/\text{cm}$  with an opacity of 0.12.

## C. RADIATION SCALING WITH CURRENT AND MASS/LENGTH

It is hoped that setting the opacity in this way (so that the computed yields agree with experiment at a single data point) will allow one to vary the other experimentally variable parameters (such as  $\mu$  and  $V_G$ ) and obtain similar agreement. If this is indeed the case, then one would feel justified in varying other parameters (such as  $a_0$ ) which are not easily changed in experiment in order to predict better experimental design. Therefore, the following series of simulations were performed to compare with similar experimental results.



Fixing  $a_0$  to the experimental value of 1.25 cm, the yield was investigated at eight values of  $V_G$  (or  $I_P$ ) with neon gas. The results for the  $K$ -shell X-ray yield  $Y_K$  with respect to variation of mass/length at each of the eight current levels is shown in Fig. 9. As mentioned several times above, there is an optimum value of  $\mu$  for each current level, varying between 15 and 45  $\mu\text{g}/\text{cm}$  (the version of the code with the skin was used). The single data point which was used to normalize the opacity to match experiment is the optimal point on the curve with  $I_P = 1.23 \text{ MA}$ . Corresponding experimental results for five current levels are shown in Fig. 10: note that, again, these yields are experimentally measured with respect to the initial gas nozzle pressure. The general trend of the curves here compares well with the simulation results: the peak yield on several experimental curves agree to within about 10% with the peaks in the simulation curves, when the current levels can be matched. This comparison can be made somewhat clearer by plotting the simulation results of Fig. 9 against pressure, instead of  $\mu$ . If one plots the optimum  $\mu$  against optimum pressure for five of the simulation curves (or interpolations of them) which roughly match the current levels of the experimental curves, one obtains the linear relationship shown in Fig. 11. This can then be used to translate the simulation curves into functions of pressure, as shown in Fig. 12, which now can be directly compared with the experimental results.

Probably the most notable difference is the relative widths of the curves: the experimentally measured radiated energy appears to be slightly less sensitive to variations in pressure (or  $\mu$ ). One explanation for the narrower curves produced by the simulation could be that the radiated energy density curves used (Fig. 7) are too narrow functions of temperature. To see this, one first needs to understand why there is an optimum  $\mu$  for fixed values of the other parameters. A simple reason based on the thermalization concept described in Section III is as follows: If one assumes that the evolution of the plasma annulus during the implosion or run-in phase (i.e., before assembly time, or thermalization) is driven by a magnetic force which is constant in time, then the kinetic energy imparted to the plasma would be the same for all values of  $\mu$ . This is because the constant force would act over the same radial distance ( $a_0 - (r_0 + w)$ ), even though the time required for run-in would

increase with larger  $\mu$ . Thus, the thermalization process would convert the same amount of kinetic energy into thermal energy and distribute it over all the particles in the core.

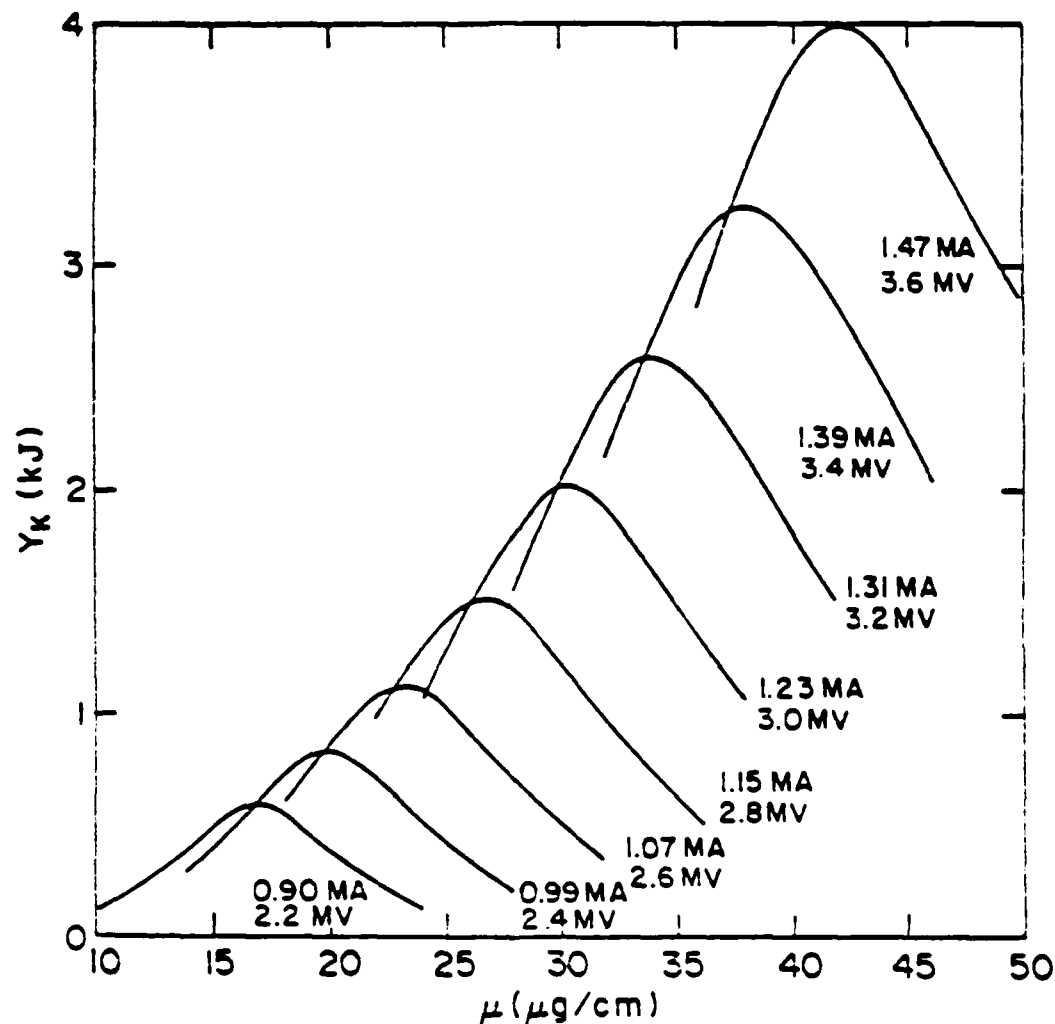


FIG. 9. Numerical results for neon  $K$ -shell radiated energy  $Y_K$  as a function of mass/length  $\mu$  for eight values of peak load current  $I_P$  (labelling the curve in MA. along with the value of the generator open circuit voltage in MV). The initial radius was fixed at  $a_0 = 1.25$  cm.

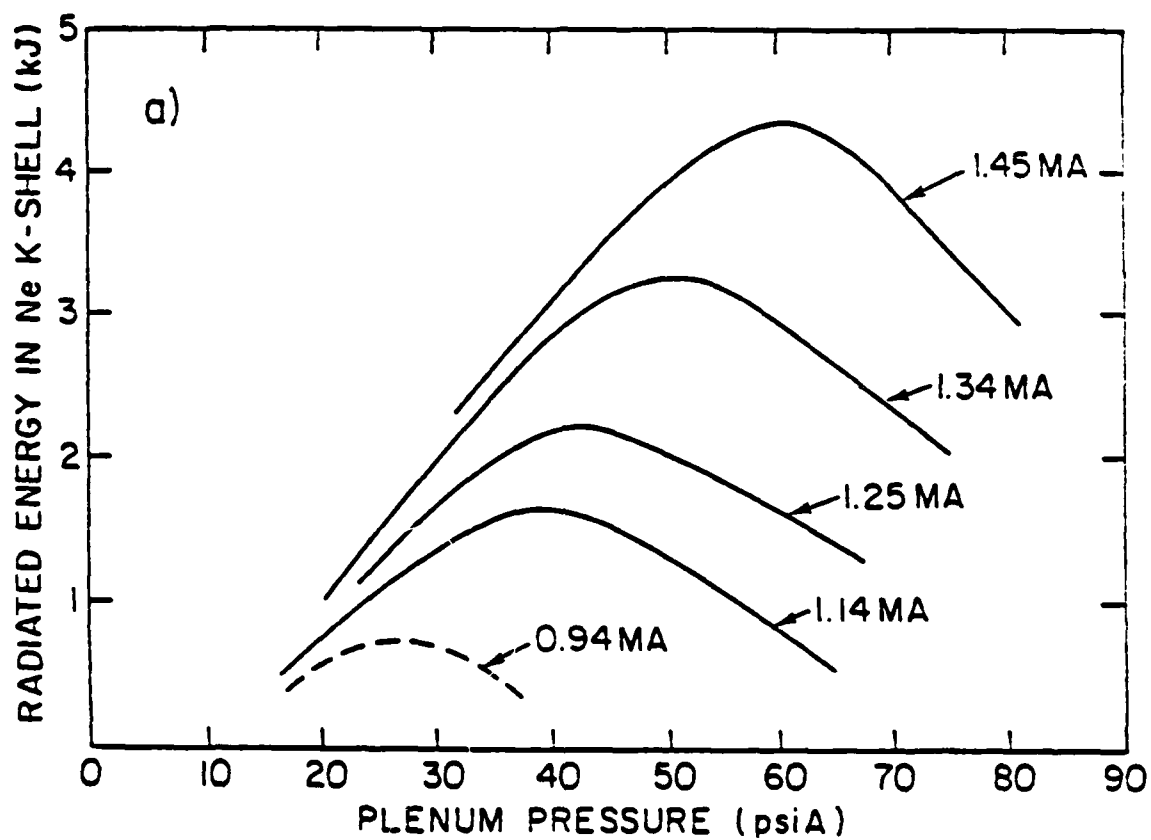


FIG. 10. Experimental results for neon  $K$ -shell radiated energy  $Y_K$  as a function of plenum pressure for five values of peak load current  $I_P$  (labelling the curve in MA). The nozzle used in experiment has a radius of 1.25 cm.

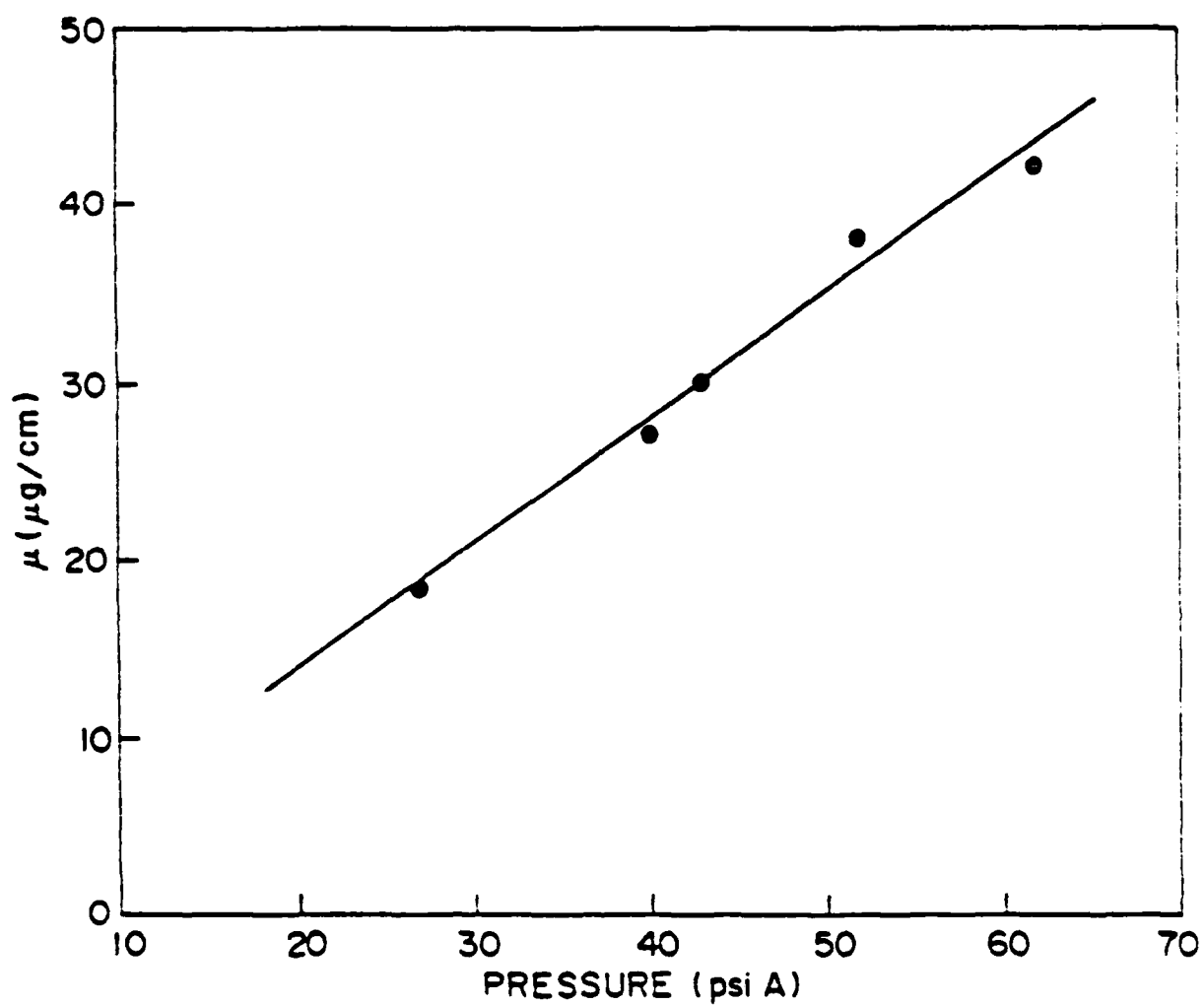


FIG. 11. Graph of optimum values of  $\mu$  against optimum values of nozzle pressure for corresponding curves (or interpolations thereof) from Figs. 9,10.

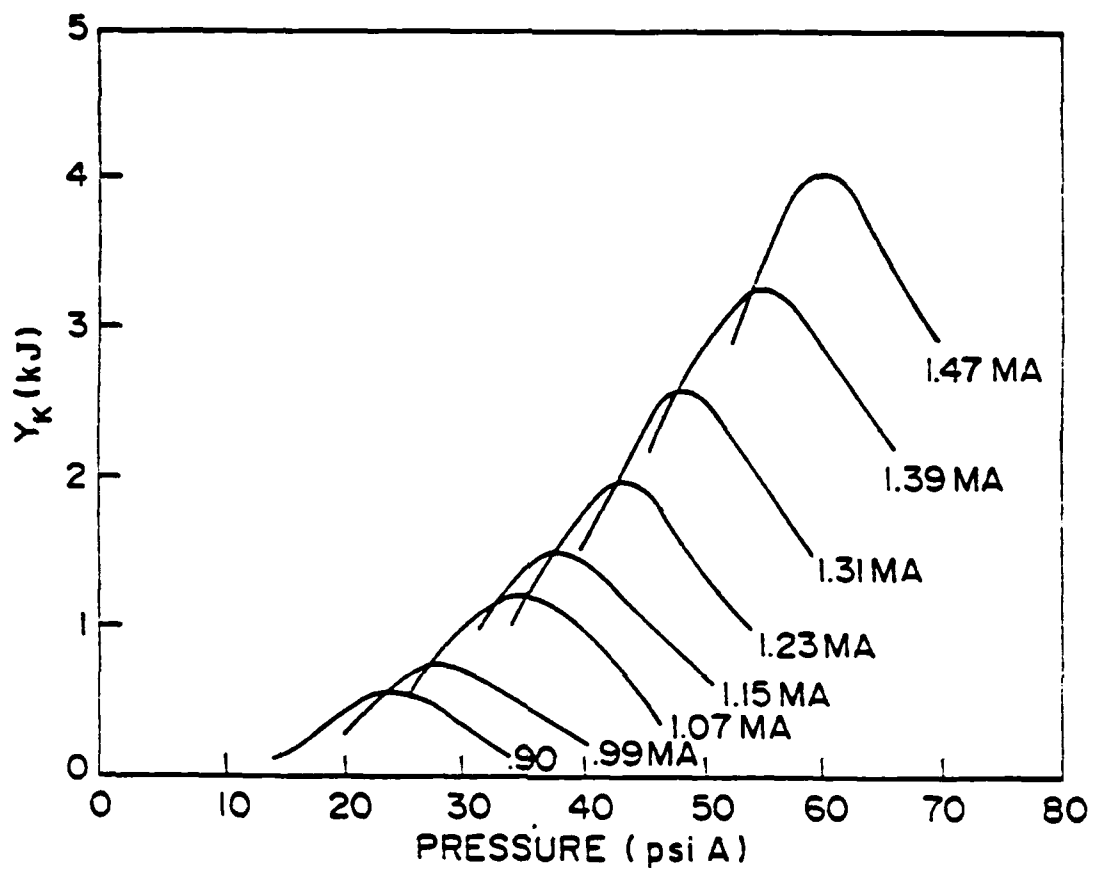


FIG. 12. Numerical results from Fig. 9 plotted in terms of nozzle pressure using the best-fit linear relationship of Fig. 11.

This is where the mass/length makes a difference: the larger the value of  $\mu$ , the more ions (and electrons) there are in the core, so the thermalization process distributes less energy per particle. Thus, for small values of  $\mu$ , the core temperature increases so much during thermalization that the resulting pressure bounces the plasma back out before it reaches a density which produces a significant amount of radiation ( $R \sim n^2$ ). Furthermore, the temperature would overshoot the optimum value for the X-ray emission. On the other hand, if  $\mu$  is very large, the temperature due to thermalization is too small for the plasma to ever reach optimum X-ray emission temperatures at pinch time, and hence only a small amount of radiation is observed. Therefore, somewhere between small values and large values of  $\mu$  there must be values where significantly more radiation is emitted.

Both the real physical system and the simple model described in this paper are of course more complicated than the explanation given above. However, what is true is that there is a delicate balance between the mass/length, the temperature achieved at pinch, the density achieved at pinch and the radiation produced: the interaction of these effects are responsible for the existence of an optimum mass/length. Because of this temperature dependence of the radiation then, the off-optimum performance can be understood also. If the radiation curves in Fig. 7 were extremely narrow in temperature, then only the optimum  $\mu$  value would radiate significantly and any case with off-optimum  $\mu$  would produce very little radiation. Thus, the widths of the yield curves in Figs. 9-12 must be related to the widths of the temperature dependence of the radiation in Fig. 7. It is evident then that the actual physical system radiates significantly over a slightly larger temperature range than that assumed in the model.

The variation of K-shell radiated energy  $Y_K$  with peak load current  $I_P$  in Figs. 9-12 is quite dramatic. In Fig. 13, we plot the value of  $Y_K$  at optimum  $\mu$  for each current level curve in Fig. 9. This log-log plot has a best fit slope of 4.02, which implies a scaling law  $Y_K \sim I^4$ . Furthermore, plotting in Fig. 14 the value of  $Y_K$  at optimum  $\mu$  against  $\mu$  for each curve in Fig. 9, one finds a  $Y_K \sim \mu^2$  scaling. These scaling laws agree with those found in experiment, shown in Fig. 15.

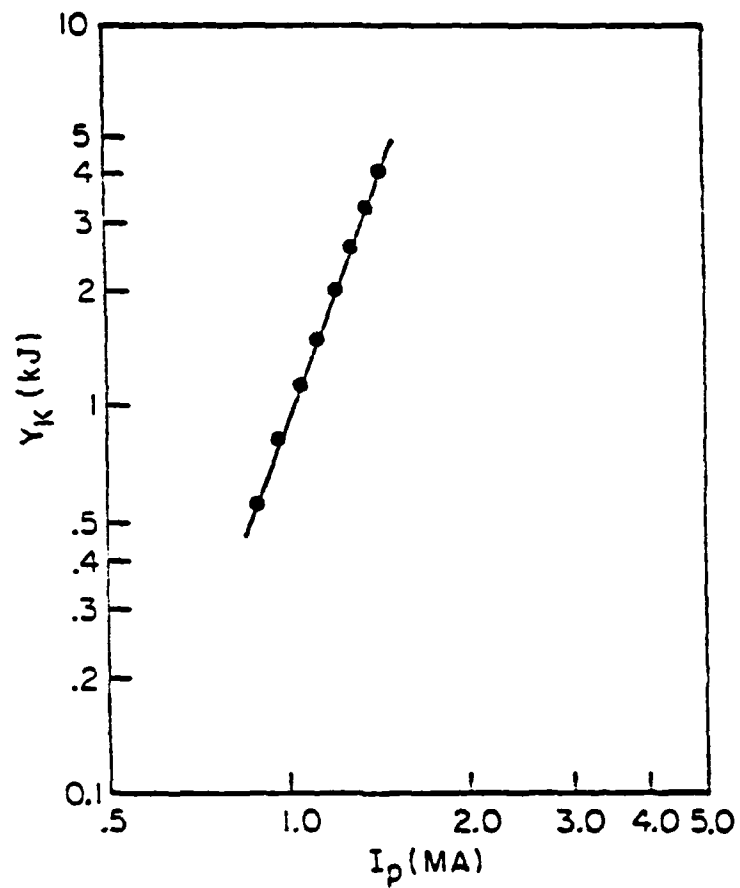


FIG. 13. For each constant-current curve in Fig. 9, the value of  $Y_K$  at optimum  $\mu$  is plotted against the value of the current  $I_p$ . The best-fit slope is 4.02.

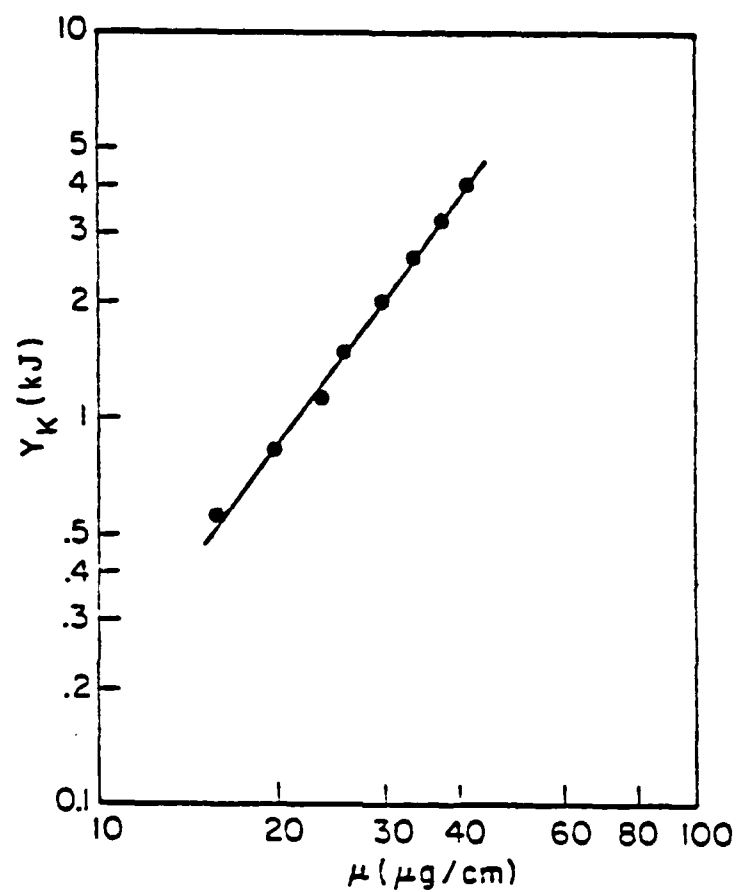


FIG. 14. For each constant-current curve in Fig. 9, the value of  $Y_K$  at optimum  $\mu$  is plotted against the value of  $\mu$ . The best-fit slope is 2.1.



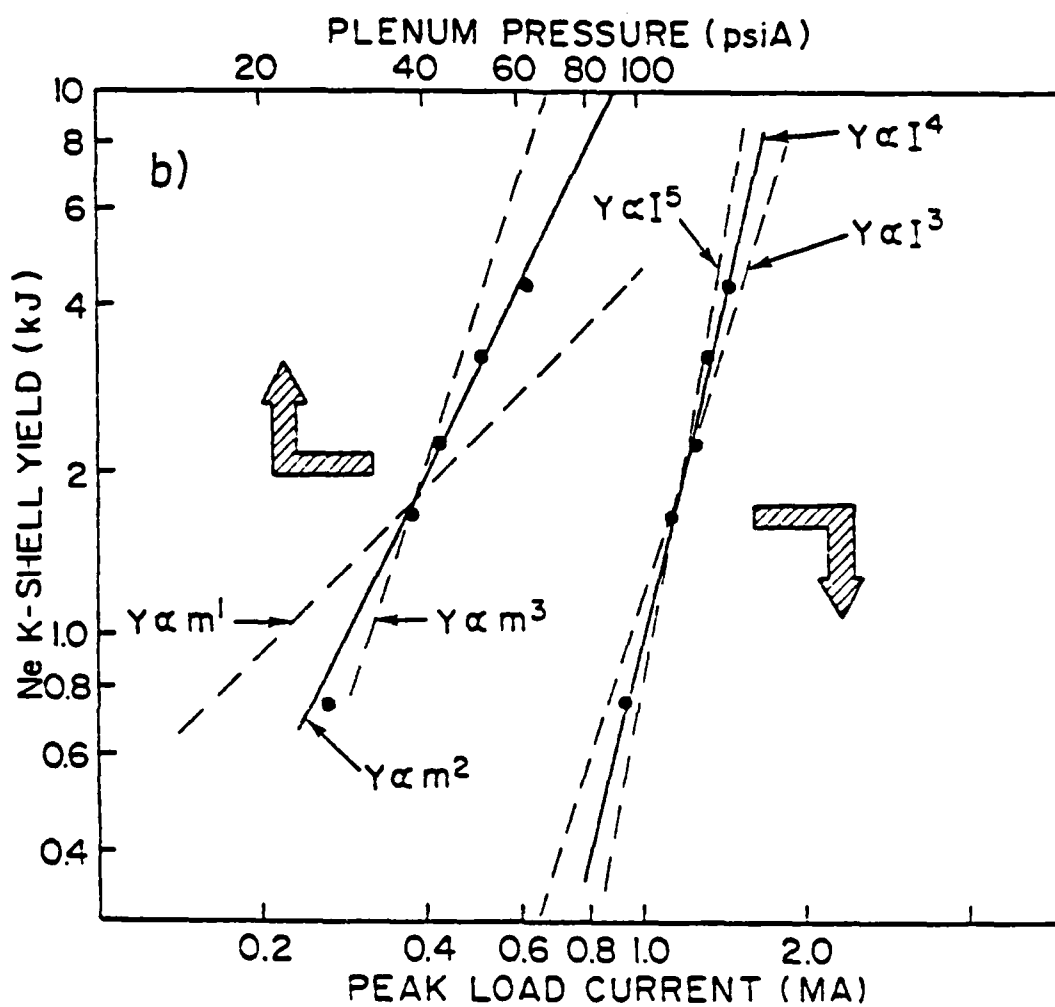


FIG. 15. Experimental scaling laws corresponding to those in Figs.13.14 using the measured results shown in Fig. 10.

Such scaling laws have been explained in the past on the basis of very simple physical arguments. These arguments, however, do not take into account the temperature dependence of the radiation and thus do not contain the concept of an optimum mass/length. In a greatly simplified version of the theory presented in Section II, the radiation can be treated as a perturbation on the dynamics of the implosion after the assembly (thermalization) time, and used to calculate curves similar to those in Fig. 9. In that theory, the ideas of optimum mass/length and the broadening of the yield curves being associated with the width of the radiation dependence on temperature are made explicit. In addition to producing the scaling laws observed above, this theory explains the presence of an optimum mass in terms of the idea of an *optimum implosion velocity* at assembly (thermalization) time: that is, the value of the optimum mass for a given current is that which reaches a particular velocity (independent of current) at assembly time. Evidence for this idea has been observed in experiment<sup>10</sup> and is provided by the numerical results shown in Fig. 16. In (16a), we plot the velocity at thermalization  $u_T$  of the optimum mass/length case against the load current from Fig. 9; in (16b),  $u_T$  for the optimum mass case is plotted against the value of  $\mu$ . That the value of  $u_T$  is indeed fairly constant in these optimum cases, however, may only indicate that the simplified treatment which predicted such a property succeeds in replacing the more complicated equations of the model which the code actually evolves. The existence of an optimum velocity in the real physical system is still an open question.

#### D EVOLUTION OF DYNAMICAL VARIABLES

As an example of the numerical solution to the equations of motion given in Section II and Appendix B, the evolution of several of the dynamical variables and related physical characteristics of the imploding plasma for a particular set of input parameters are presented in this subsection. The parameters are in fact those given in the table at the beginning of this Section, except for  $\delta_0$  which was taken to be the value of  $c/\omega_e$  for the initial density (this is actually much too small for a skin depth, as will be seen).

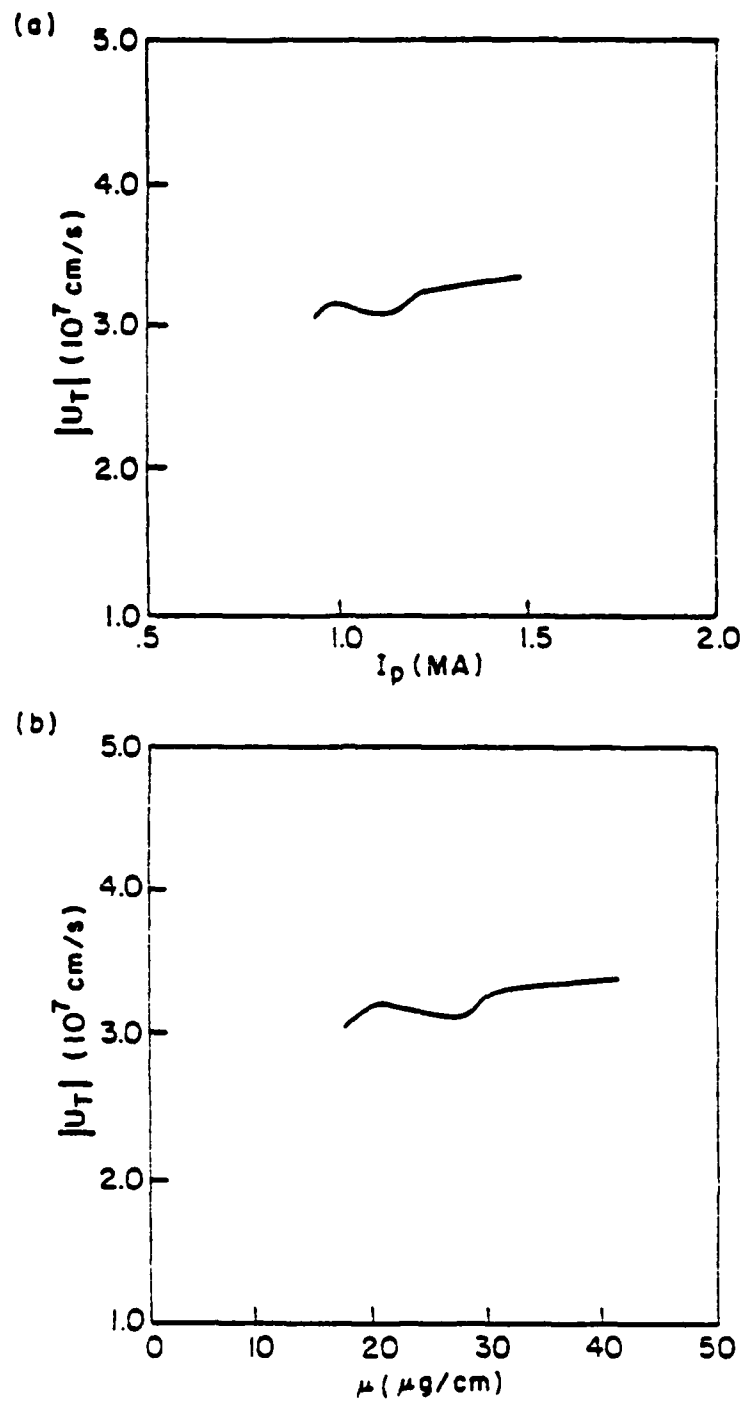


FIG. 16. For each constant-current curve in Fig. 9, we plot the velocity  $u_T$  at thermalization for the optimum mass/length case as a function of (a) the value of  $I_P$  on the curve, and (b) the value of  $\mu$  for the optimum case.

Fig. 17(a) shows the trajectory of the outer radius  $a$ , beginning at  $a_0 = 1.25$  cm, thermalizing at  $t = 106$  ns (when  $b = r_0 = 1$  mm,  $a = 4$  mm), pinching at  $t = 117$  ns and bouncing back out (although the code run of 200 ns is not long enough for it to reach the wall radius,  $r_w = 3.5$  cm). The outer radius velocity  $u(t)$  is shown in (b) accelerating to a maximum inward speed of 0.033 cm/ns at thermalization; then, with thermalization producing a significant plasma temperature and pressure (see (d)), the inward motion immediately begins to slow, passing through  $u = 0$  at pinch and finally reaching a fairly constant outward speed when the temperature and current decrease significantly. The density rises quite rapidly to a peak of about  $2.6 \times 10^{19}$  cm $^{-3}$  at pinch in (c). The core temperature history in (d) reveals the abrupt effect of the thermalization procedure: at  $t = 106$  ns,  $T_c$  rises from less than 5 eV to 158 eV (the details of the thermalization are in the example numbers used at the end of Section III). With this boost,  $T_c$  continues to rise due to compressional heating, reaching a maximum of about 460 eV near pinch. As stated earlier, this is the optimum  $\mu$  case for the present current level, and this peak temperature is in the correct range for maximum  $K$ -shell X-ray emission: the peak is reached just slightly before pinch, however, because as the temperature and density become optimum for radiation, the surge of radiation acts to cool off the plasma. This radiation pulse is shown in (e), where the solid line is the total radiated power, the dotted line (nearly invisible under the solid line) is the  $K$ -shell X-ray radiated power, and the curve marked with an "L" is the  $L$ -shell radiated power. Evidently, since the pinch temperature is appropriate for  $K$ -shell emission, this is the primary type of radiation produced. The integral of these curves over time gives a total yield of  $Y_T = 2.44$  kJ,  $Y_K = 2.01$  kJ, and  $Y_L = 0.29$  kJ; this is a  $K$ -shell efficiency of 82%. The  $L$ -shell emission occurs here only after pinch as the plasma expands and cools down through the optimum temperature ( $\sim 40$  eV) for this radiation; the reason that an  $L$ -shell pulse does not occur symmetrically before the pinch is because the (artificial) thermalization procedure suddenly jumps the temperature over this  $L$ -shell range. Fig. 17(f) shows the history of the average core ion charge state  $Z_c(t)$ , roughly following the temperature evolution. That energy is well-conserved throughout the simulation is evidenced in (g), where the solid curve is the total energy delivered to the PRS from the external circuit as a function of time:

$E_{in}(t) = \int_0^t I(t')V(t') dt'$ . The dotted curve is the sum of total kinetic energy, total core and skin thermal energies, stored magnetic field energy, and the total radiated energy as a function of time. The final value of about 5.5 kJ is composed of 2.4 kJ of radiation and 3.1 kJ of residual kinetic energy of expansion, the temperatures and magnetic field having largely fallen off (as shown in (h), where the magnetic energy  $\frac{1}{2}LI^2$  is plotted). The characteristics of the skin are shown in Figs. 17(i-k); the skin temperature rises to over 80 keV, mainly due to the fact that the skin depth (j) remains so small ( $\delta < 10^{-3}$  cm) during the run-in phase, producing a large current density and hence extreme resistive heating. Actually, the dominant heating of the skin is due to resistivity only during the first few nanoseconds of the run-in; after the temperature reaches the 10-100 eV range, compressional heating ( $\sim uT/a$ ) becomes the dominant effect. Admittedly, this degree of skin heating is quite unrealistic, but the radiation pulse from the skin (k) is insignificant compared with that from the core (the skin has much less volume), and the skin only plays the role of carrying the current. It turns out in this case, however, that the high pressure in the skin is the dominant force which bounces the plasma back out at pinch. As stated earlier, this skin effect can be investigated by varying the input parameter  $\delta_0$  which initializes the skin depth. Finally, some of the circuit parameters are shown in Figs. 17(l-o): the open circuit generator voltage trace (l) is a piecewise-linear fit to an experimental curve, the voltage across the PRS element in (m) reverses sign as the plasma bounces (due to the reversal of the impedance  $\dot{L} \sim u$  shown in (o)), and the load current flowing in the PRS has a slight hitch when pinch occurs ( $\sim 25$  ns after peak current) because of the smallness of the impedance then ( $\dot{L} \sim u \rightarrow 0$ ).

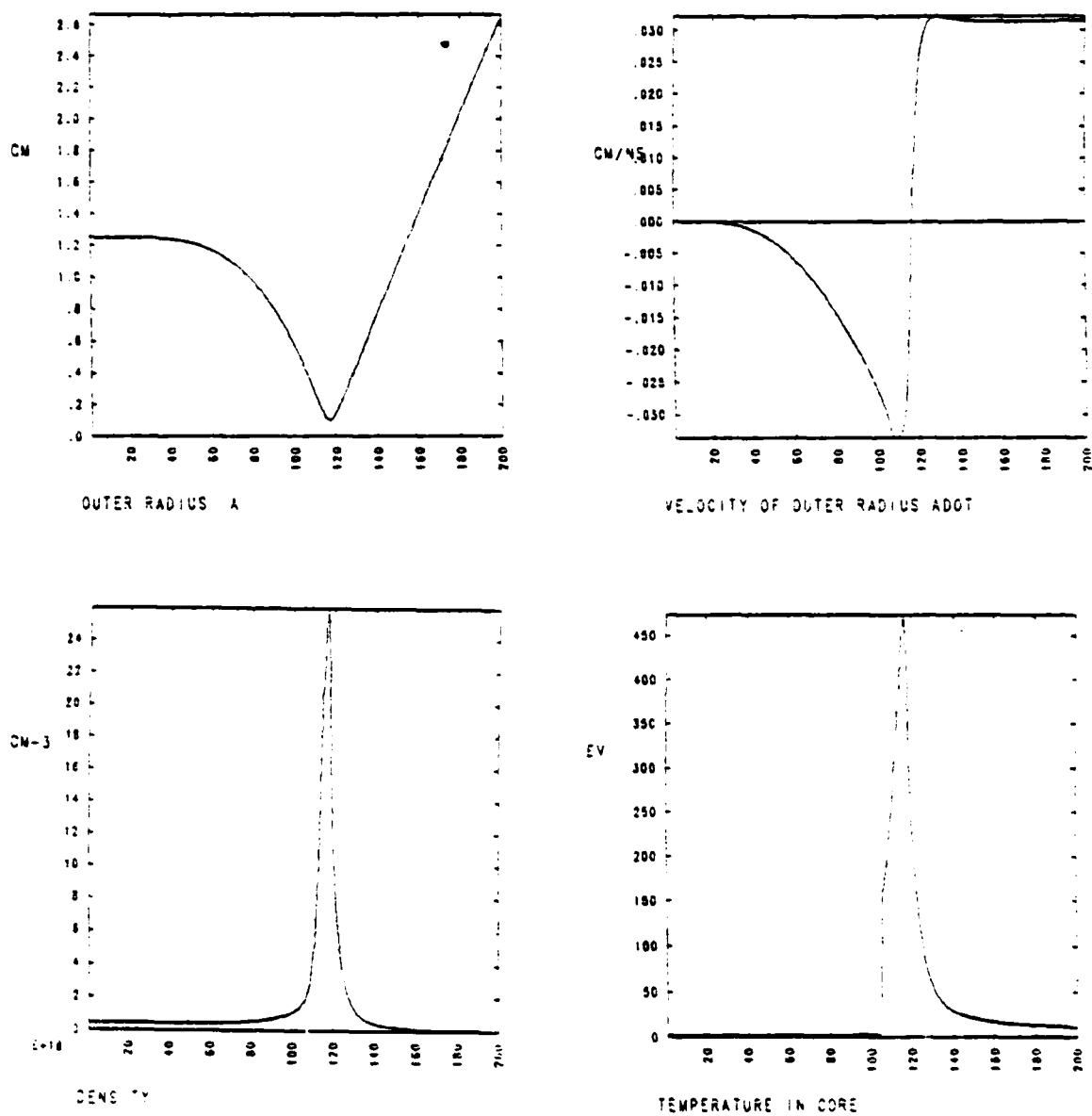


FIG. 17. Typical behavior of dynamical variables and model characteristics in optimum  $\mu$  case. (a) outer radius, (b) outer radius velocity, (c) density, (d) core temperature.

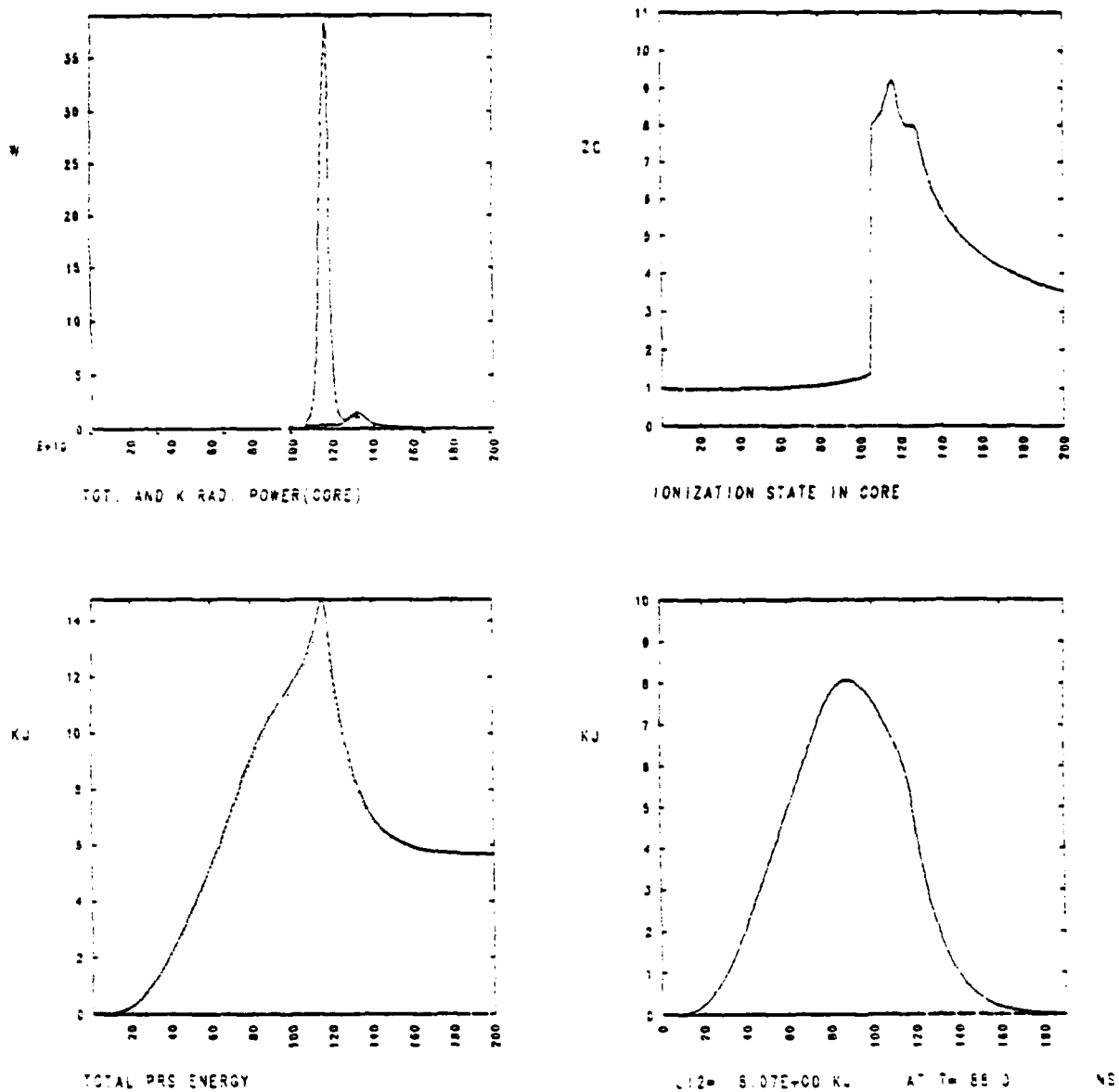


FIG. 17. (e) core radiated power, (f) core charge state, (g) total energy inventory, (h) magnetic energy.

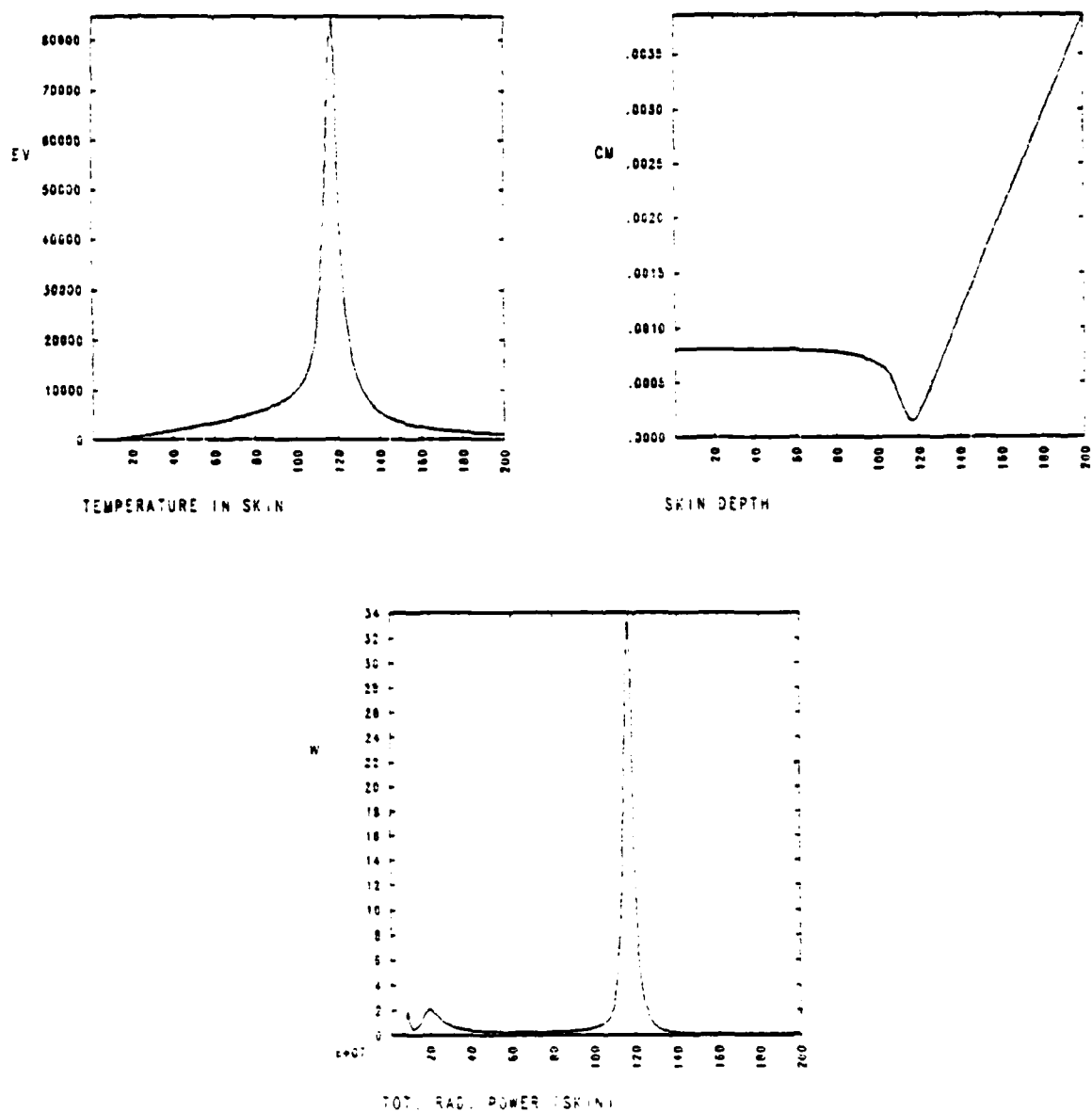
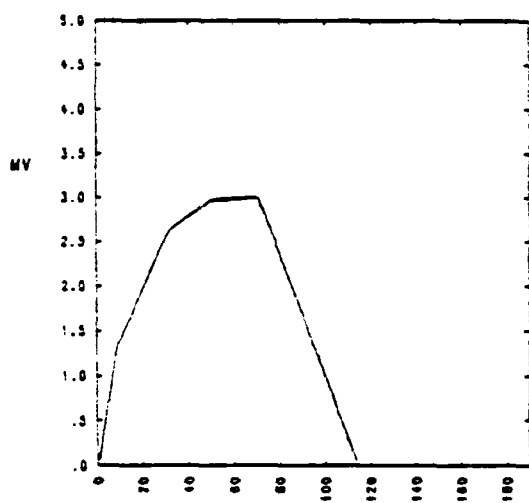


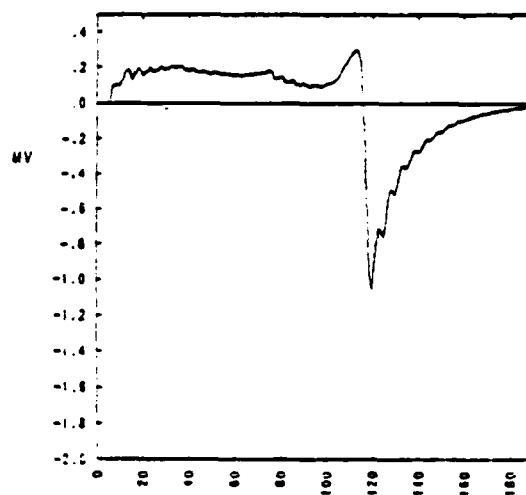
FIG. 17. (i) skin temperature, (j) skin depth, (k) skin radiated power.





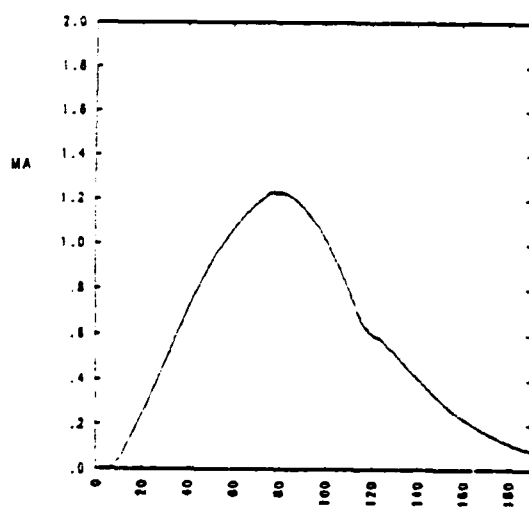
VMAX= 3.00E+00 MV AT T= 70.0

NS



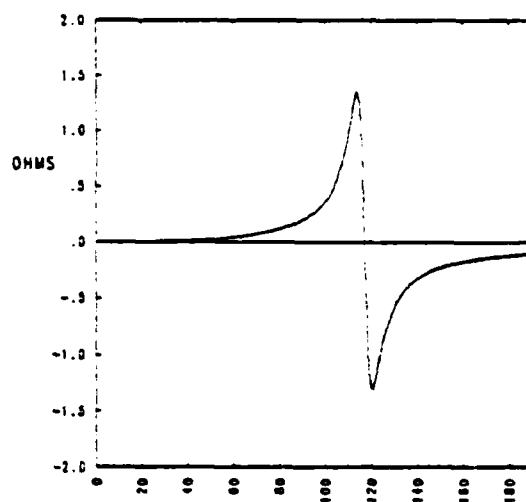
VMAX=-1.06E+00 MV AT T=120.0

NS



IMAX= 1.23E+00 MA AT T= 81.0

NS



LDOT= 1.36E+00 OHMS AT T=114.0

NS

FIG. 17. (l) generator open circuit voltage, (m) PRS voltage, (n) PRS current, (o)  $\dot{L}$ .

It is difficult to compare the evolution of the individual characteristics shown in Fig. 17 with experiment for obvious reasons: the outer radius in experiment is not well defined, time resolution of characteristics is not precise, temperature and density are difficult to measure, etc. One can, however, compare grosser features such as circuit quantities and aspects of the radiation. In Fig. 18 we show a typical comparison of (a) load current, (b)  $K$ -shell radiated power pulse, and (c)  $K$ -shell radiated energy as a function of time. While the current appears to match very well, the radiation pulse produced by the model is significantly narrower than the experimentally observed pulse. The reason for the difference between the widths of the simulation and experimental pulses in this case is only weakly related to the temperature dependence of the radiation model used in the code (radiating over a slightly larger temperature range would broaden the pulse, but the density-squared effect would still constrain the pulse to occur only over 10-30 ns around pinch time). The primary reason for the difference in pulse widths is the so-called "zipper effect": as the gas jets away from the nozzle, it tends to spread radially so that the real physical gas puff resembles more a hollow cone than a hollow cylinder. Thus, the end closest to the nozzle begins the implosion with a smaller outer radius and therefore pinches (and radiates) perhaps 10-20 nanoseconds before the end of the plasma farthest from the nozzle (with larger initial radius).<sup>11</sup> This axial dependence of the radiation emission broadens the measured pulse, although as is shown in Fig. 18(c), the total energy produced in simulation and experiment is nearly the same (note the time scale only goes to 180 ns). The "zipper effect" cannot be modelled with the present code (which assumes axial uniformity), but a slight modification which partitions the gas-puff into several independent contiguous segments (with separate properties, such as different values of  $a_0$ ,  $w$ ,  $\ell$ , and even  $\mu$ ) is being investigated in order to reproduce this phenomenon.<sup>12</sup>

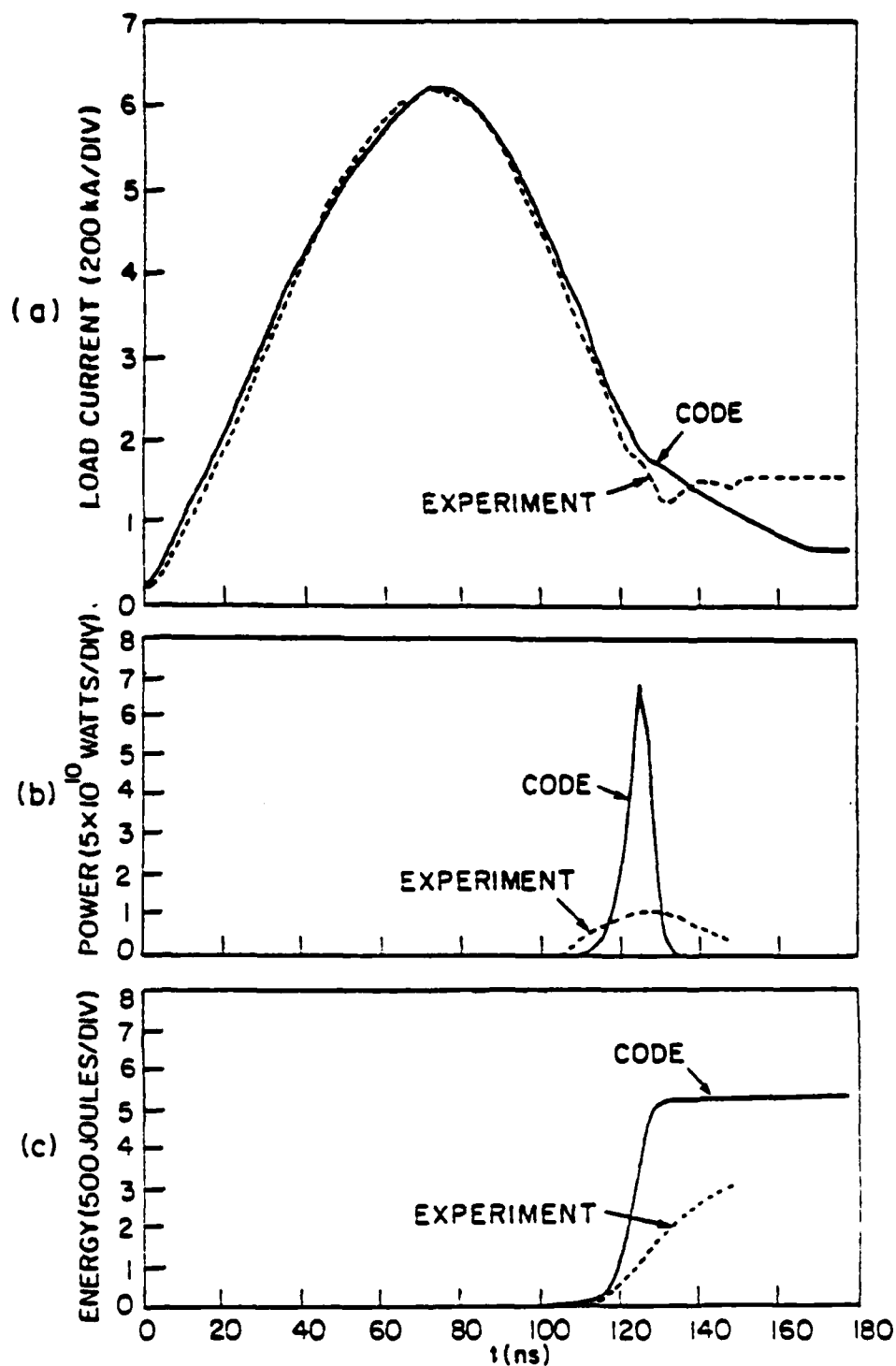


FIG. 18. Comparison of code results with experiment for neon. (a) Load current. (b) *K*-shell radiated power pulse, (c) *K*-shell radiated energy.

## E. PARAMETER OPTIMIZATION

Now that evidence has been presented which shows that this model produces results which compare satisfactorily with experimental observations when simulating current experiments, the code will be used as a tool to study parameter regimes not presently available to experiment in order to investigate optimization of design and operating parameters. One such issue has been the effect of changing the gas nozzle diameter: how would the radiation yield and efficiency depend on the initial radius of the plasma? This is a time-consuming question to answer experimentally, as a new nozzle would be required for each data point: this could be very expensive, if one does not have some idea of the appropriate sizes to try (larger or smaller? and how much?). Therefore, the following study was performed: After normalizing model parameters so that code results and experimental measurements match satisfactorily as described above, the total yield  $Y_T$  and the  $K$ -shell yield  $Y_K$  were computed (for neon) at fixed load current  $I_P = 1.2 \text{ MA}$  for different initial radii  $a_0$  as a function of mass/length  $\mu$ . The version of the code with skin was used (in fact, all runs were made with  $\delta_0 = c/\omega_e$  as in the results of the previous subsection).

The results of this investigation are shown in Fig. 19. These curves, labelled by the value of initial outer radius, clearly show a trend toward much higher yields for smaller values of  $a_0$ . For example, the  $K$ -shell yield with the  $a_0 = 1.25 \text{ cm}$  nozzle is about 2 kJ (Fig. 19(b)), whereas a nozzle with  $a_0 = 0.9 \text{ cm}$  is predicted to produce over 4 kJ. A reason for the improved behavior for smaller nozzles could be that higher densities (smaller radii) at pinch are reached. Initial values smaller than  $a_0 = 0.8 \text{ cm}$  were not systematically investigated, but it would be expected that the trend of increasing yield for decreasing nozzle radius can not continue: eventually the run-in phase before thermalization would be so short that the plasma would not acquire much kinetic energy, implying only a small amount of energy available for thermalization. Indeed, code runs with very small  $a_0$  tend to end prematurely because the outer radius has become negative: this "crashing" of the plasma onto the axis indicates that the pressure was not enough to bounce the plasma back out

after thermalization.\* The X-ray efficiency shown in Fig. 19(c) peaks at about 80% near optimum mass values, but falls off dramatically at higher values of  $\mu$ . This peak efficiency of 80% is near to what has been observed in *GAMBLE II* experiments.<sup>11</sup>

The same optimization investigation has also been performed with the version of the code which does not have a skin. The results for  $Y_T$ ,  $Y_K$  and  $(Y_K/Y_T)$  are shown in Fig. 20. Again, the trend toward better yield at smaller nozzle radius is apparent, although the magnitude of the yields at different  $a_0$  are somewhat higher than in Fig. 18. Also, as mentioned above, the optimum value of  $\mu$  for a given current and initial radius is computed to be slightly larger in the version without skin than in the one with skin. Furthermore, in this version, almost all computer runs with  $a_0 < 1$  cm resulted in the "crashed" mode ( $a < 0$ ) described above. Thus, as stated above, the general behavior of the radiated yields and X-ray efficiency in Fig. 20 are similar to those in Fig. 18; the reason for the discrepancies between the results produced by the two versions of the code is being investigated.

Some of the results of this optimization study are summarized in the Table in Fig. 21.

---

\* This condition is signaled by the error message "trouble=1." The remainder of the system will continue to a normal termination with the PRS fixed at its last non-negative value of  $a$  and with  $u = 0$ . Actually, there are many reasons for such an occurrence, including a scenario where the increasing density as the radius decreases causes more radiation, which cools the plasma, decreasing the pressure, which allows a further reduction of radius, higher density and more radiation, etc. It is believed, however, that because the equations evolved by the code admit conservation of energy, this condition should not occur and might be corrected by decreasing the timestep. In any case, the data produced by such a run should not be considered.

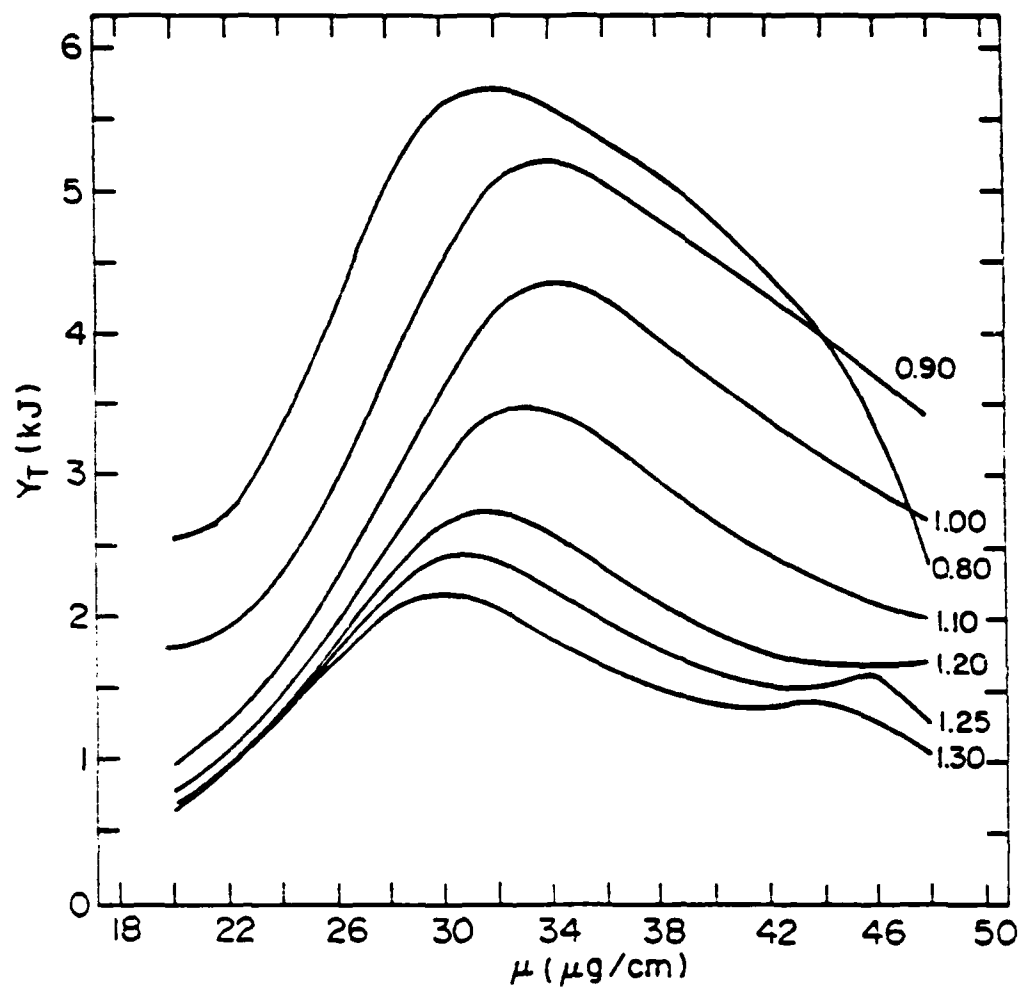


FIG. 19. Results of nozzle radius optimization study. With load current fixed at 1.2 MA, *opacity* = 0.25 (code version with skin), the radiation yield was computed as a function of mass/length  $\mu$  for various values of initial radius  $a_0$ . (a) Total radiated energy,  $Y_T$ .

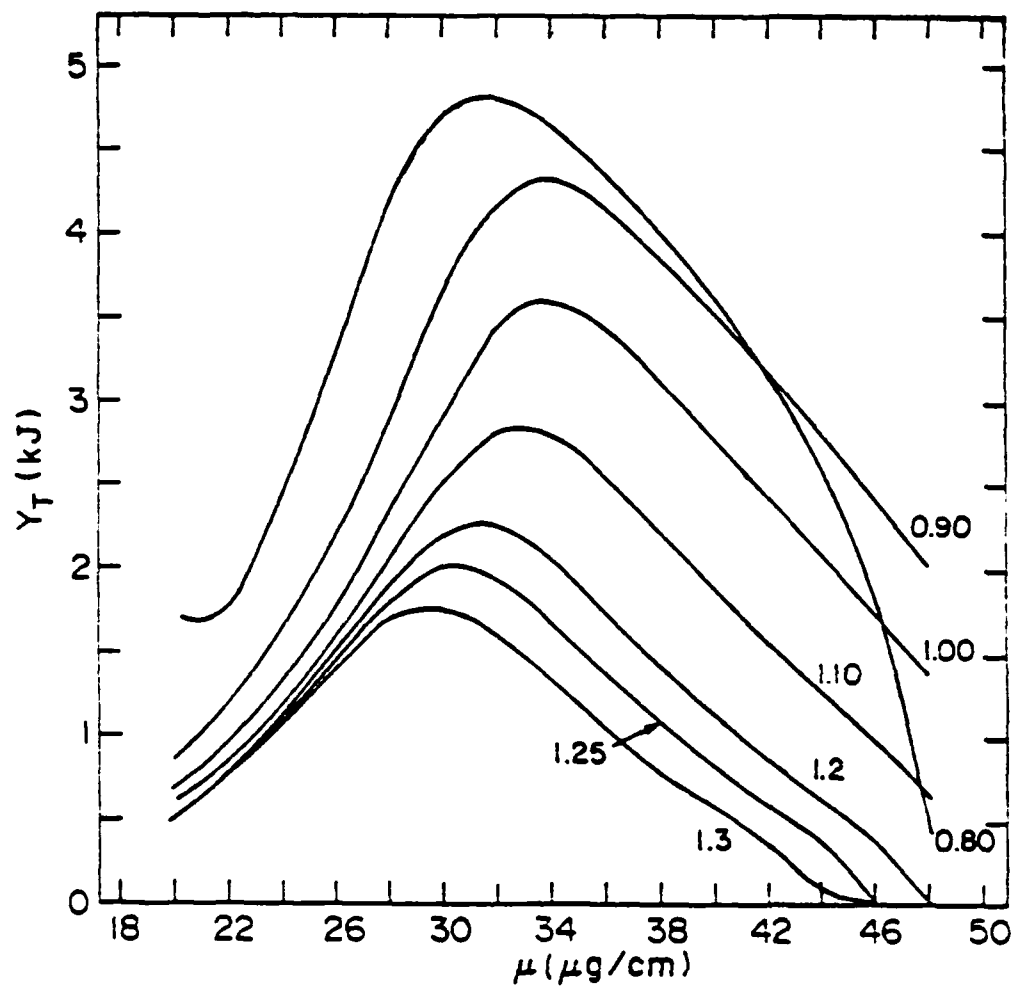


FIG. 19. (b)  $K$ -shell radiated energy,  $Y_K$ .

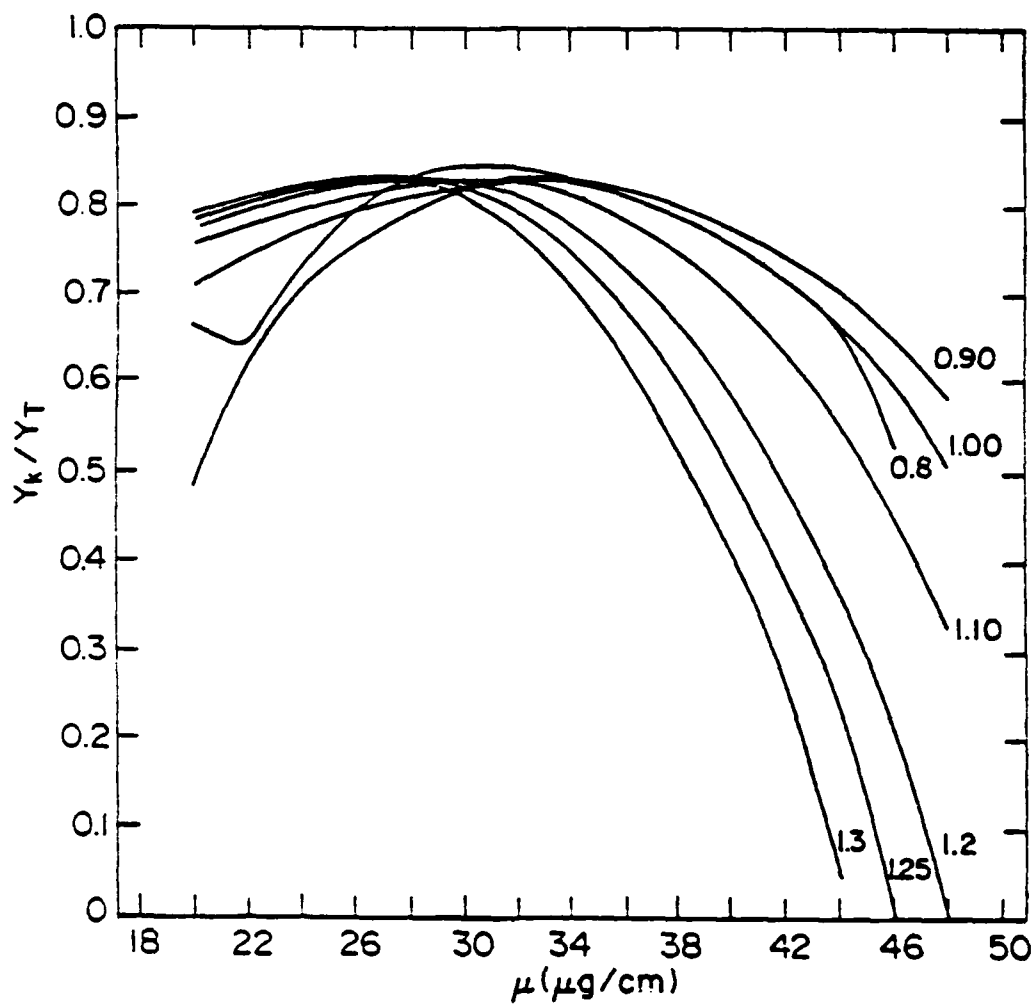
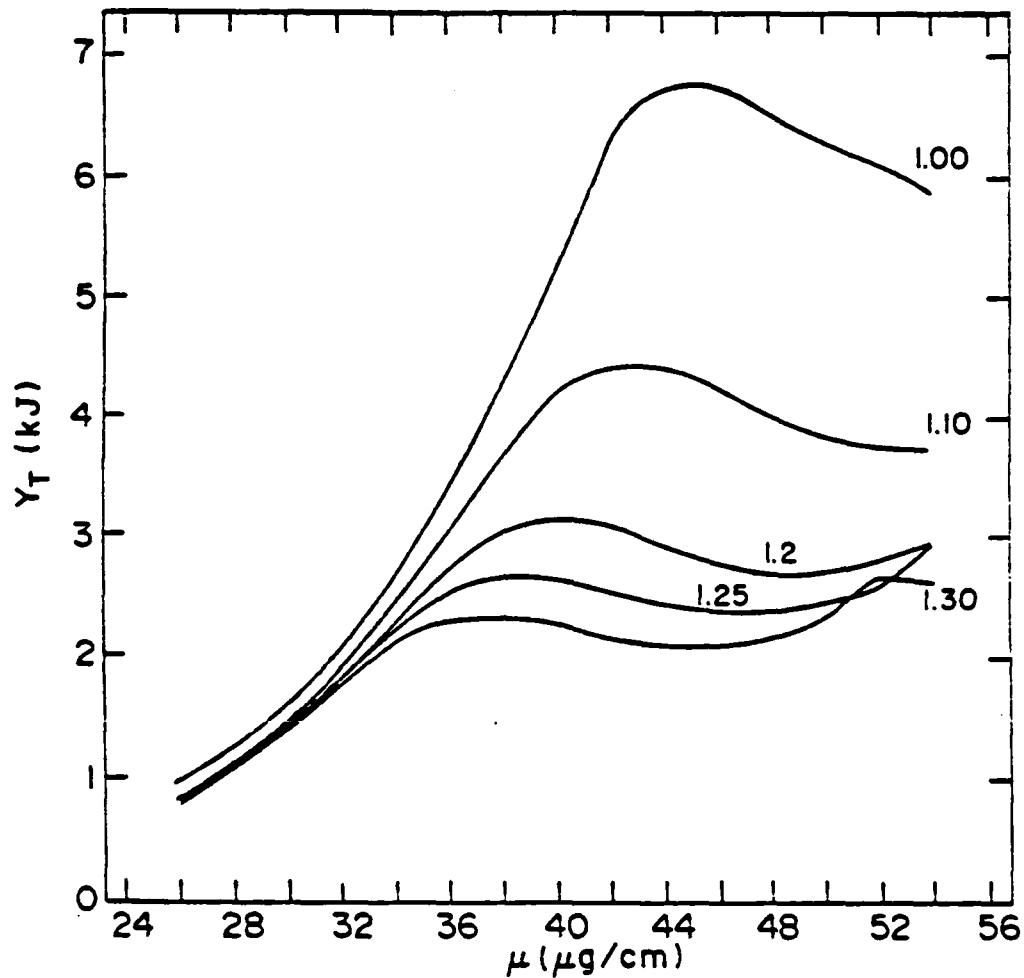


FIG. 19. (c) X-ray efficiency,  $Y_K/Y_T$ .





**FIG. 20.** Results of nozzle radius optimization study. With load current fixed at 1.2 MA, *opacity* = 0.12 (code version without skin), the radiation yield was computed as a function of mass/length  $\mu$  for various values of initial radius  $a_0$ . (a) Total radiated energy,  $Y_T$ .

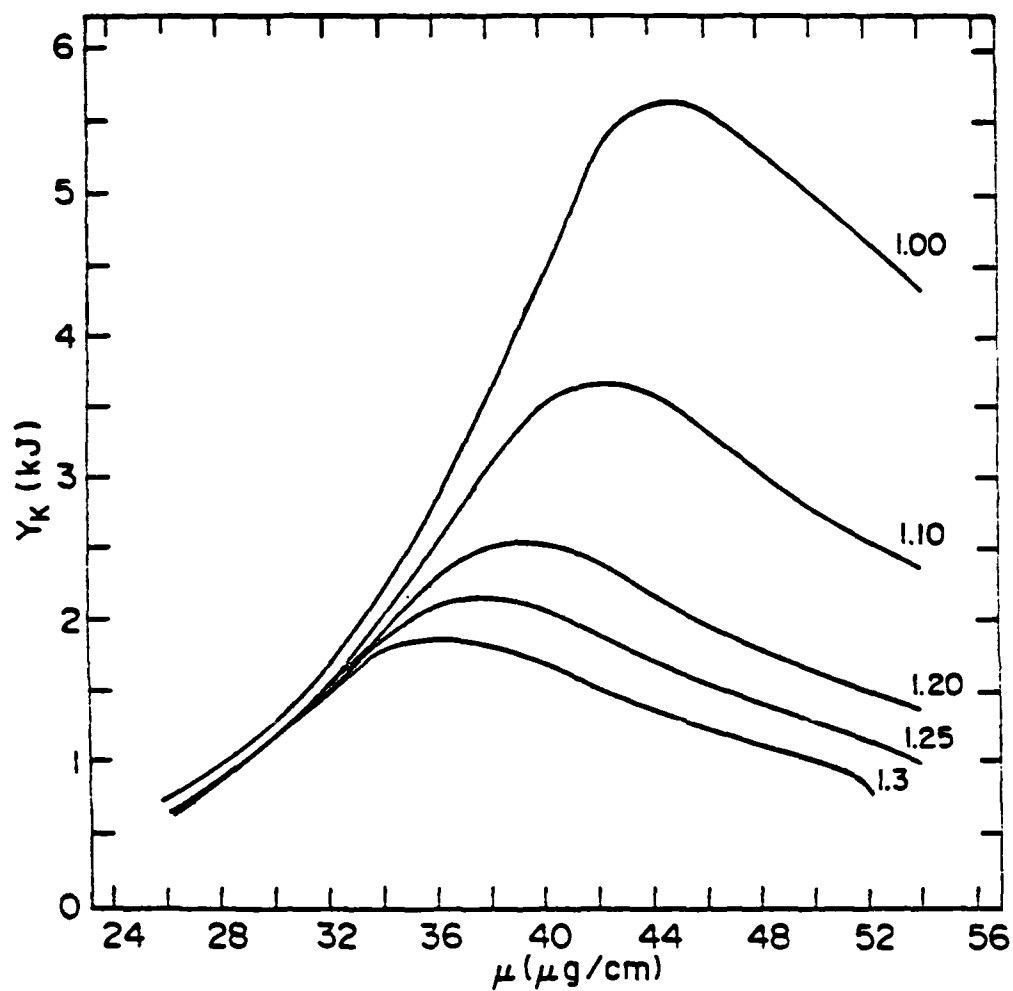


FIG. 20. (b)  $K$ -shell radiated energy,  $Y_K$ .

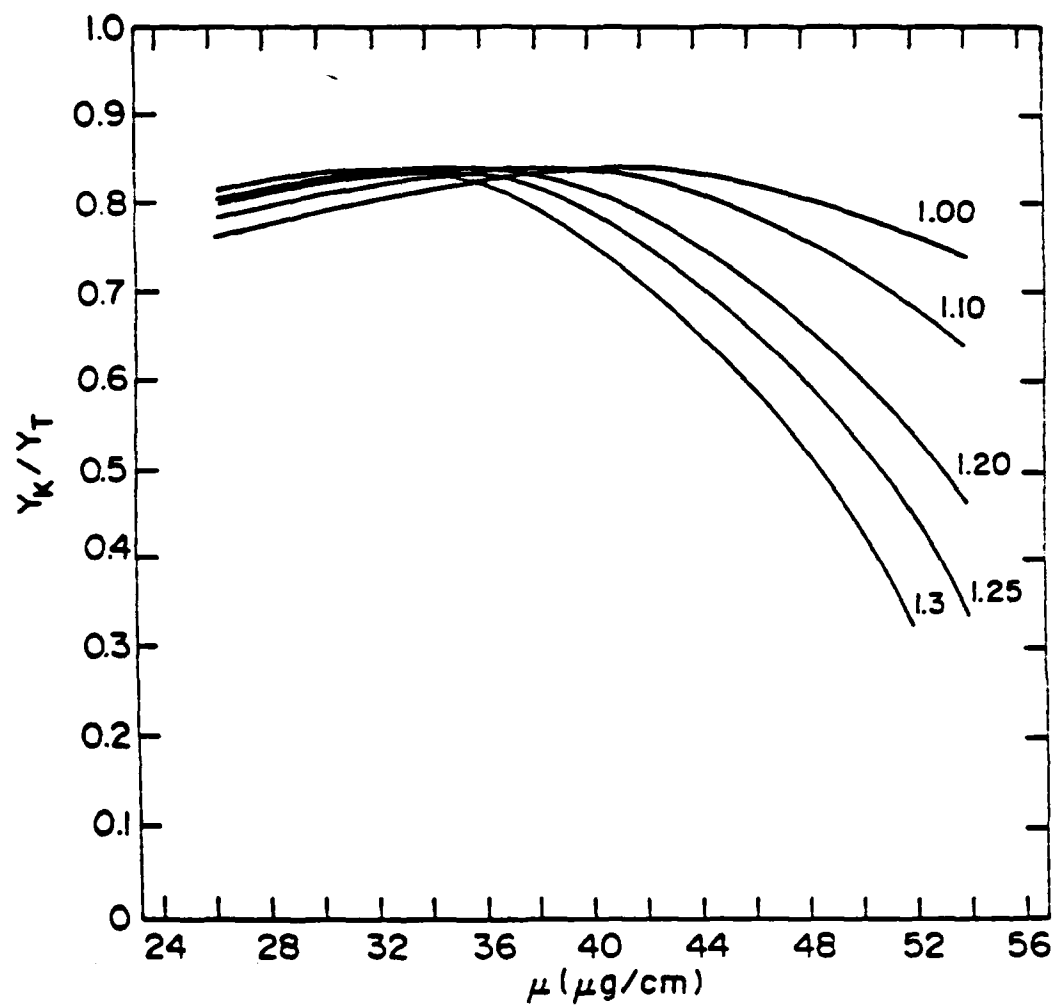


FIG. 20. (c) X-ray efficiency,  $Y_K/Y_T$ .

With Skin (opacity=0.25)	Initial Radius (cm)	Mass/ Length ( $\mu\text{g}/\text{cm}$ )	K-line Yield (kJ)	K-line eff.	Assembly Time (ns)	Pinch Time (ns)	Pinch Radius (cm)	Pinch Density ( $10^{18}\text{cm}^{-3}$ )	Assembly Velocity (cm/ns)	Core Pinch Temp (eV)	Skin Pinch Temp (kV)	Peak Current (MA)	Pinch Current (MA)
Present	1.25	30	2.0	82%	106	116	0.10	2.6	0.033	476	85	1.23	0.85
Optimum	0.80	32	4.8	84%	79	90	0.01	18.0	0.025	440	220	1.17	0.90
Without Skin (opacity=0.12)	1.00	34	3.6	83%	94	105	0.07	6.5	0.029	440	130	1.21	0.80
Present	1.00	44	5.6	84%	100	114	0.05	20.0	0.026	450	N/A	1.22	0.85
	1.25	38	2.2	82%	114	126	0.08	5.1	0.028	410	N/A	1.24	0.45

FIG. 21. Summary of results of nozzle radius optimization study.

## VI. CONCLUSION

A simple theoretical model of an imploding gas-puff plasma radiation source has been described, as well as its implementation in the computer code *IMplode*. The purpose of the model is to be able to compute the amount of radiation produced by the imploding plasma, yet it was intended to be simple enough to be used in design and parameter optimization studies. Based on single fluid MHD theory, these equations were averaged over the volume of the gas to obtain ordinary differential equations for the outer radius, the outer radius velocity and the average temperature of the plasma. Results of sophisticated atomic physics ionization and radiation calculations were used to compute the radiated power density as a function of plasma temperature and density. The results of the code compare well with existing experimental observations, justifying its use in predicting optimal design parameters. Thus, the main result is that a reduction in gas-nozzle radius from the current value of 1.25 cm to 0.9 cm could perhaps double the *K*-shell X-ray yield for a neon gas-puff. Indeed, this has been recently observed in experiment.<sup>13</sup>

## ACKNOWLEDGMENTS

We are indebted to the NRL *GAMBLE II* experimental group for many helpful discussions; we are particularly grateful for the assistance and criticism of S. J. Stephanakis and F. C. Young. We would also like to thank D. Duston, R. E. Terry, J. Davis, T. Cochran, and J. P. Apruzese for useful discussions of the work and for their cooperation in supplying the necessary atomic physics and radiation data, without which this work would not have been possible. In particular, D. Duston provided data from collisional radiative equilibrium calculations and R. E. Terry provided the piecewise numerical fits to these data for the equation of state, average ion charge state and radiated power density.

## APPENDIX A: CONSERVATION OF ENERGY

In this Appendix, it is shown that the total energy of the  $Z$ -pinch is conserved by the equations of motion derived in Section II, in that the total amount of energy put into the system can be accounted for. Thus, one expects the following to hold

$$\frac{d}{dt}(K + U_c + U_s + \frac{1}{2}LI^2) + V_c\bar{R}_c + V_s\bar{R}_s = P_{in} = I\dot{\Phi} + I^2\mathcal{R}. \quad (A.1)$$

Here again,  $K$  is the total kinetic energy of the imploding plasma (governed by (12,16)),  $U_c$  and  $U_s$  are the total thermal energies of the core and skin respectively, including ionization energy (governed by (25,26)), and  $V_c\bar{R}_c + V_s\bar{R}_s$  is the total radiated power from the skin and the core. The new quantities here are the energy in the magnetic field  $\frac{1}{2}LI^2$  expressed in terms of the inductance  $L$ , and the power  $P_{in}$  delivered to the system from the external circuit. The latter includes both the resistive heating  $I^2\mathcal{R}$  of the skin and the effect of the time-varying magnetic flux  $\Phi$ . In terms of the inductance, the  $I\dot{\Phi}$  can be expressed as

$$I\dot{\Phi} = I(LI)' = \frac{1}{2}L(I^2)' + \dot{L}I^2 = (\frac{1}{2}LI^2)' + \frac{1}{2}\dot{L}I^2. \quad (A.2)$$

Thus, the power into the magnetic field can be eliminated from both sides of (A.1), and the energy actually coupled into the plasma should satisfy

$$\frac{d}{dt}(K + U_c + U_s) + V_c\bar{R}_c + V_s\bar{R}_s = \frac{1}{2}\dot{L}I^2 + I^2\mathcal{R}. \quad (A.3)$$

Collecting the evolution equations (16,26) and using the definitions (25) for the thermal energies in (23), we have the following

$$\begin{aligned} \dot{K} &= \frac{2u}{a+b}(N_c\bar{T}_c + N_s\bar{T}_s) + (vJB), \\ \dot{U}_c &= \frac{3}{2}N_c\dot{\bar{Q}}_c = -\frac{2u}{a+b}N_c\bar{T}_c - V_c\bar{R}_c, \\ \dot{U}_s &= \frac{3}{2}N_s\dot{\bar{Q}}_s = -\frac{2u}{a+b}N_s\bar{T}_s - V_s\bar{R}_s + V_s\eta J^2. \end{aligned} \quad (A.4)$$

Adding these together, the pressure (temperature) terms evidently cancel and one finds

$$\frac{d}{dt}(K + U_c + U_s) + V_c\bar{R}_c + V_s\bar{R}_s = (vJB) + V_s\eta J^2. \quad (A.5)$$

Of course, the more general equations (16,20) give the same result when added. From the definition of the resistance  $\mathcal{R}$  in terms of the resistivity  $\eta$ ,  $\mathcal{R} = \ell\eta/A_s$  (where  $A_s$  is the cross-sectional area of the skin), one can readily identify the resistive heating term in (A.5) with  $I^2\mathcal{R}$ . Therefore, comparison of (A.5) with (A.3) indicates that the evolution equations (A.4) conserve energy (as stated above) if one can identify the  $(\underline{vJB})$  term with the coupled energy  $\frac{1}{2}\dot{L}I^2$ . That this is the case should be easy to determine since the velocity profile, current density and magnetic field are all known quantities.

Before proceeding to calculate the  $(\underline{vJB})$  term, however, we comment on the result. By actual calculation, one finds

$$\frac{1}{c} \int dV_s \underline{v} \cdot (\underline{J} \times \underline{B}) = \frac{1}{2}(\dot{L}_0 + \dot{L}_1)I^2. \quad (\text{A.6})$$

Here,  $L_0$  is the inductance of the plasma annulus inside the cylindrical cavity assuming that the plasma is a perfect conductor (so that the current flows in a skin of zero thickness); thus, this is the usual vacuum coaxial inductance  $L_0 = (2\ell/c^2) \ln(r_w/a)$ . The correction  $L_1$  to the inductance represents the contribution from the fact that the skin has a finite thickness  $\delta$ . As this correction term is generally small, however, for simplicity in the code implementation the imploding Z-pinch has been presented to the exterior circuit as an element with the coaxial inductance  $L_0$ . The  $(\underline{vJB})$  term in the equation of motion (16,17) is therefore simply set equal to  $\frac{1}{2}\dot{L}_0 I^2$  in order to be consistent. Thus, the plasma evolves in such a way that the energy it receives from the exterior circuit is exactly that delivered to it as computed by the current and voltage on the element.

Omitting the details, the  $(\underline{vJB})$  term is

$$\begin{aligned} \frac{1}{c} \int dV_s \underline{v} \cdot (\underline{J} \times \underline{B}) &= -\frac{2\pi\ell}{c} \int_x^a r dr \left( \frac{A_1}{r} + A_2 r \right) \times \\ &\quad \left( \frac{I}{\pi(a^2 - x^2)} \right) \left[ \frac{2I}{c(a^2 - x^2)} \left( r - \frac{x^2}{r} \right) \right] \\ &= -\frac{\ell I^2}{c^2} \frac{u}{a} \left[ 1 - \frac{b}{a+b} + \frac{2a}{a+b} \frac{ab}{a^2 - x^2} \left( 1 - \frac{2x^2 \ln(a/x)}{a^2 - x^2} \right) \right]. \end{aligned} \quad (\text{A.7})$$

With  $\dot{L}_0 = -(2\ell/c^2)(u/a)$ , comparison of (A.7) with (A.6) gives the formula for

$$\dot{L}_1 = \frac{2\ell}{c^2} \frac{u}{a} \left[ \frac{b}{a+b} - \frac{2a}{a+b} \frac{ab}{a^2 - x^2} \left( 1 - \frac{2x^2 \ln(a/x)}{a^2 - x^2} \right) \right]. \quad (\text{A.8})$$

Now, defining the inductance in terms of the energy  $\frac{1}{2}LI^2$  in the magnetic field,<sup>14</sup> one obtains

$$\begin{aligned}\frac{1}{2}LI^2 &\equiv \int dV (B^2/8\pi) \\ &= \frac{\ell I^2}{c^2} \ln(r_w/a) + \frac{2\pi\ell}{8\pi} \int_x^a r dr B^2(r) \\ &\equiv \frac{1}{2}(L_0 + \Delta L)I^2,\end{aligned}\tag{A.9}$$

where the contribution from the skin gives the extra inductance

$$\Delta L \equiv \frac{2\ell}{c^2} \frac{1}{a^2 - x^2} \left( \frac{1}{4}(a^2 + x^2) - x^2 + \frac{x^4 \ln(a/x)}{a^2 - x^2} \right).\tag{A.10}$$

The time-derivative of (A.10) is

$$(\Delta L)' = \frac{2\ell}{c^2} \frac{u}{a} \left[ \frac{b}{a+b} - \frac{2a}{a+b} \frac{ab}{a^2 - x^2} \left( 1 - \frac{2x^2 \ln(a/x)}{a^2 - x^2} \right) \right],\tag{A.11}$$

again using  $\dot{x} = v(x)$ . This is the same as (A.8), so that one can correctly identify the  $(vJB)$  term as the inductively coupled energy  $\frac{1}{2}LI^2$ .



## APPENDIX B: EQUATIONS OF MOTION

In this Appendix, the expressions for the ordinary differential equations actually implemented and evolved in the subroutine *IMPLode* are given. As derived in Section II, these are five coupled equations governing the outer radius  $a$ , the outer radius velocity  $u$ , the average total "thermal" energy of the core  $\bar{Q}_c$  and skin  $\bar{Q}_s$ , and the core radius  $x = a - \delta$ .

### A. EQUATIONS WITH SKIN

By definition, the first equation is simply  $\dot{a} = u$ . The equation for the velocity  $u$  now comes from the kinetic energy equation (16,17); with the use of (7) for the velocity profile  $v(r)$ , the total kinetic energy  $K$  can be computed and then differentiated with respect to time. Thus,

$$\begin{aligned} K &\equiv \int dV \frac{1}{2} \rho v^2(r) \\ &= \pi \rho \ell \int_b^a r dr (A_1^2 r^{-2} + 2A_1 A_2 + A_2^2 r^2) \\ &= \frac{\mu \ell}{a^2 - b^2} [A_1^2 \ln(a/b) + A_1 A_2 (a^2 - b^2) + \frac{1}{4} A_2^2 (a^4 - b^4)]. \end{aligned} \quad (\text{B.1})$$

This expression remains valid even after the assembly time (when the inner radius  $b \rightarrow 0$ ) provided the correct values of  $A_1$  and  $A_2$  are used:

$$\begin{array}{cc} A_1 & A_2 \\ b > 0: & \frac{abu}{a+b} \quad \frac{u}{a+b} \\ b = 0: & 0 \quad \frac{u}{a} \end{array} \quad (\text{B.2})$$

With these values in (B.1), the kinetic energy before and after  $b \rightarrow 0$  takes the following forms:

$$b > 0: \quad K = \frac{1}{4} \mu \ell u^2 \left[ 1 + \frac{2ab}{(a+b)^2} + \frac{4a^2 b^2 \ln(a/b)}{(a-b)(a+b)^3} \right], \quad (\text{B.3a})$$

$$b = 0: \quad K = \frac{1}{4} \mu \ell u^2. \quad (\text{B.3b})$$

Now, differentiating these with respect to time one obtains

$$b > 0: \quad \dot{K} = \frac{\mu \ell u \dot{u}}{2(a+b)^2} \left[ a^2 + b^2 + 4ab + \frac{4a^2 b^2 \ln(a/b)}{a^2 - b^2} \right] + \frac{\mu \ell u^3}{2(a+b)^3} \left[ a^2 + b^2 - 4ab + \frac{4ab(a^2 + b^2 - ab) \ln(a/b)}{a^2 - b^2} \right], \quad (\text{B.4a})$$

$$b = 0: \quad \dot{K} = \frac{1}{2} \mu \ell u \dot{u}, \quad (\text{B.4b})$$

where the constant thickness condition  $\dot{a} = \dot{b} \equiv u$  has been used. Note that as  $b \rightarrow 0$ , the coefficient of  $\dot{u}$  in (B.4a) smoothly goes into the correct expression (B.4b) for  $b = 0$ ; the  $u^3$  term, however, does not vanish in this limit but goes to the value  $u^3/a$ . This discrepancy is of course due to the abrupt qualitative change in the velocity profile as  $b \rightarrow 0$ .

The terms on the right-hand side of (16) are now calculated as follows: the pressure terms are

$$\begin{aligned} \frac{2u}{a+b} N_c \bar{T}_c &= \frac{2u \bar{T}_c}{a+b} n V_c (\bar{Z}_c + 1) \\ &= 2\mu \ell u \bar{T}_c \frac{(\bar{Z}_c + 1)}{m_i(a+b)} \frac{x^2 - b^2}{a^2 - b^2}, \end{aligned} \quad (\text{B.5})$$

$$\begin{aligned} \frac{2u}{a+b} N_s \bar{T}_s &= \frac{2u \bar{T}_s}{a+b} n V_s (\bar{Z}_s + 1) \\ &= 2\mu \ell u \bar{T}_s \frac{(\bar{Z}_s + 1)}{m_i(a+b)} \frac{a^2 - x^2}{a^2 - b^2}, \end{aligned} \quad (\text{B.6})$$

while the  $(vJB)$  term is simply replaced by

$$(vJB) \rightarrow \frac{1}{2} \dot{L}_0 I^2 = -\frac{\ell}{c^2} \frac{u}{a} I^2. \quad (\text{B.7})$$

(see the discussion in Appendix A).

Combining these expressions in the form (17), the equation for the outer radius velocity is

$$\dot{u} = -(C_2/C_1)u^2 + (C_{3c}/C_1)\bar{T}_c + (C_{3s}/C_1)\bar{T}_s - (C_4/C_1)I^2, \quad (\text{B.8})$$

where the coefficients are

While  $b > 0$

$$C_1 = \frac{1}{(a+b)^2} \left[ a^2 + b^2 + 4ab + \frac{4a^2b^2 \ln(a/b)}{a^2 - b^2} \right], \quad (\text{B.9a})$$

$$C_2 = \frac{1}{(a+b)^3} \left[ a^2 + b^2 - 4ab + \frac{4ab(a^2 + b^2 - ab) \ln(a/b)}{a^2 - b^2} \right], \quad (\text{B.9b})$$

$$C_{3c} = \frac{4(\bar{Z}_c + 1)}{m_i(a+b)} \frac{x^2 - b^2}{a^2 - b^2}, \quad (\text{B.9c})$$

$$C_{3s} = \frac{4(\bar{Z}_s + 1)}{m_i(a+b)} \frac{a^2 - x^2}{a^2 - b^2}, \quad (\text{B.9d})$$

$$C_4 = \frac{2}{\mu c^2 a}. \quad (\text{B.9e})$$

While  $b = 0$

$$C_1 = 1, \quad (\text{B.10a})$$

$$C_2 = 0, \quad (\text{B.10b})$$

$$C_{3c} = \frac{4(\bar{Z}_c + 1)}{m_i a} \frac{x^2}{a^2}, \quad (\text{B.10c})$$

$$C_{3s} = \frac{4(\bar{Z}_s + 1)}{m_i a} \frac{a^2 - x^2}{a^2}, \quad (\text{B.10d})$$

$$C_4 = \frac{2}{\mu c^2 a}. \quad (\text{B.10e})$$

Again, all coefficients go smoothly as  $b \rightarrow 0$  into their values at  $b = 0$ , except for  $C_2$ . Note that these "coefficients" are really time-dependent: they depend on the values  $a$ ,  $b = a - w$ ,  $x$ ,  $\bar{Z}_c(\bar{T}_c)$  and  $\bar{Z}_s(\bar{T}_s)$ .

The equations governing the thermal energies of the core and skin given in (26) are of the form

$$\dot{Q}_c = -C_{5c} u \bar{T}_c + C_{6c} I^2 - C_{7c}, \quad (\text{B.11a})$$

$$\dot{Q}_s = -C_{5s} u \bar{T}_s + C_{6s} I^2 - C_{7s}, \quad (\text{B.11b})$$

where the coefficients are

$$C_{5c,5s} = -\frac{4}{3(a+b)}, \quad (\text{B.12a})$$

$$C_{6c} \equiv 0, \quad (\text{B.12b})$$

$$C_{6s} = \frac{2m_i}{3\pi\mu\sigma(\bar{Z}_s + 1)} \frac{a^2 - b^2}{(a^2 - x^2)^2}, \quad (\text{B.12c})$$

$$C_{7c,7s} = \frac{2\pi m_i(a^2 - b^2)}{3\mu(\bar{Z}_{c,s} + 1)} \bar{R}_{c,s}. \quad (\text{B.12d})$$

These expressions are all valid even with  $b = 0$ . As prescribed in the model, no current flows in the core (B.12b). The conductivity  $\sigma$  used in the skin (B.12c) is taken to be just the Spitzer conductivity

$$\sigma = 1.96 \times 9.0 \times 10^{13} \frac{\bar{T}_s^{3/2}}{\lambda \bar{Z}_s},$$

where the Coulomb logarithm  $\lambda$  is

$$\lambda = \begin{cases} 23.0 - \ln(n \bar{Z}_s^{3/2} \bar{T}_s^{-3/2}) & \text{for } \bar{T}_s < 10\text{eV} \\ 24.0 - \ln(n^{1/2} \bar{Z}_s^{1/2} \bar{T}_s^{-1}) & \text{for } \bar{T}_s > 10\text{eV} \end{cases}$$

These quantities are computed at each time-step. The radiated power density  $\bar{R}_{c,s}$  for the skin and the core is computed as a function of the density and temperature of each region (see Section IV).

The final equation of motion is the condition that the core radius  $x$  (or boundary between the core and the skin, see Fig. 1) move with the fluid velocity  $v(x)$  at that radius:

$$\dot{x} = A_1 x^{-1} + A_2 x, \quad (\text{B.13})$$

where the appropriate values of  $A_1$  and  $A_2$  from (B.2) are used. Combining (B.8,B.11,B.13), the five evolution equations are

$$\dot{a} = u \quad (\text{B.14a})$$

$$\dot{u} = -(C_2/C_1)u^2 + (C_{3c}/C_1)\bar{T}_c + (C_{3s}/C_1)\bar{T}_s - (C_4/C_1)I^2, \quad (\text{B.14b})$$

$$\dot{\bar{Q}}_c = -C_{5c}u\bar{T}_c + C_{6c}I^2 - C_{7c}, \quad (\text{B.14c})$$

$$\dot{\bar{Q}}_s = -C_{5s}u\bar{T}_s + C_{6s}I^2 - C_{7s}, \quad (\text{B.14d})$$

$$\dot{x} = A_1 x^{-1} + A_2 x. \quad (\text{B.14e})$$

These equations are integrated in the main routine *IMPLode* using a simple Euler method ( $y_{n+1} = \dot{y}_n \Delta t + y_n$ ) with all quantities on the right-hand sides of (14) computed at each time-step from (B.2,B.9,B.10,B.12).

The current  $I$  flowing in the plasma radiation source load element is computed by the transmission line simulation from the voltage values on either end of the element divided by the load impedance. This impedance  $Z_L$  is taken to be the impedance of a *purely inductive* element, using the expression for a coaxial transmission line:  $Z_L \equiv Z_0 \ln(r_w/a)$ . The coefficient  $Z_0$  for a standard vacuum transmission line is  $(2/c)$ , so that when the transmission line inductance  $L_0 = (2\ell/c^2) \ln(r_w/a)$  is divided by  $Z_L$  one obtains the vacuum element transit time  $\tau_L = (L_0/Z_L) = (\ell/c)$ . For implementation in the transmission line simulation, however, the gas-puff is represented to the remainder of the circuit as an element which is only one time-step  $\Delta t$  long. Therefore, with  $\tau_L \equiv \Delta t = (L_0/Z_L)$ , one finds the appropriate (artificial) value of  $Z_0$  to be  $Z_0 = (2/c)(\ell/c\Delta t)$ . This is artificial in that the impedance is larger (or smaller) than the vacuum impedance by a factor of  $(v_S/c)$ , where  $v_S = (\ell/\Delta t)$  is the speed of a signal which traverses the element of length  $\ell$  in one time-step. For the standard *GAMBLE II* gas-puff,  $\ell = 4\text{cm}$  and the usual simulation time-step is  $\Delta t = 0.1\text{ns}$ , which gives  $v_S = (4/3)c$ .

Aside from this technical point about the characteristic impedance of the inductive element, it is important to note that this treatment excludes the effect of the energy dissipation in the load due to the resistive heating of the skin (B.11,B.12c). That is, the skin is allowed to gain energy due to  $I^2/\sigma$  but this energy is not removed from the circuit by a corresponding series impedance of the form  $\mathcal{R} = (\ell/\sigma A_s) \approx (\ell/2\pi\sigma a\delta)$ , where  $A_s = \pi(a^2 - x^2)$  is the cross-sectional area of the skin. In most cases, this energy sink is negligible in terms of total energy conservation (see Appendix A), even though it can be responsible for heating the skin to anomalously high temperatures (see Section V). In other cases, however, the dissipation is significant and can cause large departures from total energy conservation; if this occurs, one should either account for the loss by incorporating a series resistance  $\mathcal{R}$  as above, or turn off the skin resistive heating term in (B.11b) (i.e., set  $C_{6s} = 0$  by letting  $\sigma \rightarrow \infty$ ). If the latter method is chosen (as was done in some of the results of Section V), then there

is really no difference between the equations (B.11) for the skin and core thermal energies. Thus, one is led to consider a simpler model which has no skin as described below.

## B. EQUATIONS WITHOUT SKIN

Since the magnetic force term ( $\sim I^2$ ) in (B.14b) is computed using (B.7) which ignores the presence of a skin, one can set the skin depth to be zero implying  $x = a - \delta \rightarrow a$  in (B.9,B.10). Now the equations of motion are for just  $a$ ,  $u$ , and  $\bar{Q}_c$ :

$$\dot{a} = u, \quad (\text{B.15a})$$

$$\dot{u} = -(C_2/C_1)u^2 + (C_{3c}/C_1)\bar{T}_c - (C_4/C_1)I^2, \quad (\text{B.15b})$$

$$\dot{\bar{Q}}_c = -C_{5c}u\bar{T}_c - C_{7c}, \quad (\text{B.15c})$$

where the coefficients are given by

While  $b > 0$

$$C_1 = \frac{1}{(a+b)^2} \left[ a^2 + b^2 + 4ab + \frac{4a^2b^2 \ln(a/b)}{a^2 - b^2} \right], \quad (\text{B.16a})$$

$$C_2 = \frac{1}{(a+b)^3} \left[ a^2 + b^2 - 4ab + \frac{4ab(a^2 + b^2 - ab) \ln(a/b)}{a^2 - b^2} \right], \quad (\text{B.16b})$$

$$C_{3c} = \frac{4(\bar{Z}_c + 1)}{m_i(a+b)}, \quad (\text{B.16c})$$

$$C_4 = \frac{2}{\mu c^2 a}, \quad (\text{B.16d})$$

$$C_{5c} = -\frac{4}{3(a+b)}, \quad (\text{B.17e})$$

$$C_{7c} = \frac{2\pi m_i(a^2 - b^2)}{3\mu(\bar{Z}_c + 1)} \bar{R}_c. \quad (\text{B.17f})$$

While  $b = 0$

$$C_1 = 1, \quad (\text{B.18a})$$

$$C_2 \equiv 0, \quad (\text{B.18b})$$

$$C_{3c} = \frac{4(\bar{Z}_c + 1)}{m_i a}, \quad (\text{B.18c})$$

$$C_4 = \frac{2}{\mu c^2 a}, \quad (\text{B.18d})$$

$$C_{5c} = -\frac{4}{3(a+b)}, \quad (\text{B.19e})$$

$$C_{7c} = \frac{2\pi m_i (a^2 - b^2)}{3\mu(\bar{Z}_c + 1)} \bar{R}_c. \quad (\text{B.19f})$$

### C. SUMMARY OF VARIABLES

Finally, the equations in Section II were derived using Gaussian units even though experimentalists measure most external circuit quantities in mks units. Therefore, for purposes of clarification of several constant conversion factors that are to be found in the code, we list here the physical quantities and the units in which they are cast for purposes of calculation in the code and on output for comparison with experiment:

Quantity	Definition	Calculation Units	Output Units
$a$	outer radius	cm	cm
$b$	inner radius	cm	cm
$\delta$	skin depth	cm	cm
$I$	current	statamps	megamps
$K$	kinetic energy	ergs	kilojoules
$l$	length	cm	cm
$L$	inductance	nanohenries	nanohenries
$m$	mass	gm	gm
$\mu$	mass/length	gm/cm	$\mu\text{g/cm}$
$n$	density	$\text{cm}^{-3}$	$\text{cm}^{-3}$
$P_{\text{rad}}$	radiated power	eV/ns	Watts
$Q$	"thermal" energy	eV	kilojoules
$R$	radiated power density	$\text{eV/cm}^3\text{-ns}$	$\text{W/cm}^3$
$\sigma$	conductivity	$\text{s}^{-1}$	$\text{s}^{-1}$
$T$	temperature	eV	eV
$u$	outer velocity	cm/ns	cm/ns
$V$	volume	$\text{cm}^3$	$\text{cm}^3$
$w$	annulus width	cm	cm
$z$	core radius	cm	cm
$Y$	yield	kilojoules	kilojoules
$Z_L$	impedance	ohms	ohms

## References

- <sup>1</sup>S. J. Stephanakis, S. W. McDonald, R. A. Meger, P. F. Ottinger, F. C. Young, C. G. Mehlman, J. P. Apruzese and R. E. Terry, *Bull. Amer. Phys. Soc.* **29**, 1232 (1984); S. J. Stephanakis, J. P. Apruzese, P. G. Burkhalter, J. Davis, R. A. Meger, S. W. McDonald, C. G. Mehlman, P. F. Ottinger and F. C. Young, to be published in *Appl. Phys. Lett.*
- <sup>2</sup>S. W. McDonald, P. F. Ottinger, R. E. Terry and S. J. Stephanakis, *Bull. Am. Phys. Soc.* **29**, 1329 6S18 (1984).
- <sup>3</sup>A similar model has been used by P. Kepple, C. Agritellis, R. Clark, J. Davis and D. Duston, *Bull. Am. Phys. Soc.* **29**, 1329 6S15 (1984). See also J. Davis, C. Agritellis, D. Duston, *NRL Memorandum Report #5615* (1985), ADA157456 (Simplode: An Imploding Gas Puff Plasma Model I. Neon).
- <sup>4</sup>J. Guillory and R. E. Terry, *Defense Nuclear Agency Report #DNA 5234F* (1980).
- <sup>5</sup>S. I. Braginskii, in *Reviews of Plasma Physics* Vol. 1, Consultants Bureau. New York (1975), pg. 275.
- <sup>6</sup>R. E. Terry, private communication. See also R. E. Terry, J. Davis, D. Duston, *Bull. Am. Phys. Soc.* **29**, 1329 6S14 (1984).
- <sup>7</sup>J. Davis, private communication.
- <sup>8</sup>D. D. Hinshelwood, *NRL Memorandum Report #5185* (1983), ADA135024 (Bertha — A Versatile Transmission Line and Circuit Code).
- <sup>9</sup>R. E. Terry, *ZDIPR Analysis of Gamble II Implosion Events*, Technical Report 6, pg. 128 in *JAYCOR Report #J206-85-002/6243* (1985).
- <sup>10</sup>S. L. Wong, private communication.
- <sup>11</sup>S. J. Stephanakis, J. R. Boller, D. D. Hinshelwood, S. W. McDonald, C. G. Mehlman, P. F. Ottinger and F. C. Young, *IEEE Int. Conf. on Plasma Science* (Pittsburgh, PA. June 1985).
- <sup>12</sup>S. W. McDonald, P. F. Ottinger, S. J. Stephanakis and F. C. Young, *Bull. Am. Phys. Soc.* **30**, 1389 (1985).



<sup>13</sup>S. J. Stephanakis, S. W. McDonald, P. F. Ottinger, J. R. Boller, V. E. Scherrer and F. C. Young, *Bull. Am. Phys. Soc.* **30**, 1389 (1985).

<sup>14</sup>For volume distributed currents, this is the appropriate definition of the inductance, as opposed to a definition in terms of the magnetic flux. See D. Corson and P. Lorrain, *Introduction to Electromagnetic Fields and Waves*, W. H. Freeman (1962), pg. 245.

# DISTRIBUTION LIST

Director		Commander	
Defense Nuclear Agency		Harry Diamond Laboratory	
Washington, DC 20305		2800 Powder Mill Rd.	
Attn: TISI Archives	1 copy	Adelphi, MD 20783	
TITL Tech. Library	3 copies	(CNWDI-INNER ENVELOPE: ATTN: DELHD-RBH)	
J. Z. Farber (RAEV)	1 copy	Attn: DELHD-NP	1 copy
J. Benson	1 copy	DELHD-RCC-J.A. Rosando	1 copy
C. Schubert	1 copy	DRXDO-RBH- J. Agee	1 copy
E. E. Stobbs	1 copy	DRXDO-TI-Tech Lib.	1 copy
Air Force Office of Scientific Research		Defense Technical Information Center	
Physics Directorate		Cameron Station	
Bolling AFB, DC 20332		5010 Duke Street	
Attn: H. Pugh	1 copy	Alexandria, VA 22314	
R.J. Barker	1 copy	Attn: T.C.	2 copy
Air Force Weapons Laboratory, AFSC		JAYCOR, Inc.	
Kirtland, AFB, NM 87117		205 S. Whiting Street	
Attn: NTYP (W. L. Baker)	1 copy	Alexandria, VA 22304	
Atomic Weapons Research Establishment		Attn: D. D. Hinshelwood	1 copy
Building H36		E. V. Weber	1 copy
Aldermaston, Reading RG 7 4PR		Kaman Tempo	
United Kingdom		816 State Street (P.O. Drawer 99)	
Attn: J. C. Martin	1 copy	Santa Barbara, CA 93102	
Boeing Company, The		Attn: DASIAC	
P.O. Box 3707		Lawrence Berkeley Laboratory	
Seattle, WA 98124		Berkeley, CA 94720	
Attn: Aerospace Library	1 copy	Attn: D. Keefe	1 copy
Brookhaven National Laboratory		Lawrence Livermore National Laboratory	
Upton, NY 11973		P.O. Box 808	
Attn: A. F. Maschke	1 copy	Livermore, CA 94550	
BMO/EN		Attn: Tech. Info. Dept. L-3	1 copy
Norton AFB, CA		D. J. Meeker	
Attn: ENSN	1 copy	Los Alamos National Laboratory	
Cornell University		P.O. Box 1663	
Ithaca, NY 14850		Los Alamos, NM 87545	
Attn: D. A. Hammer	1 copy	Attn: M. Gillispie/Theo. Div.	1 copy
R. N. Sudan	1 copy	Massachusetts Institute of Technology	
		Cambridge, MA 02139	
		Attn: R. C. Davidson	1 copy
		G. Bekefi	1 copy

Maxwell Laboratories, Inc. 9244 Balboa Avenue San Diego, CA 92123 Attn: M. Montgomery M. Gersten	1 copy 1 copy	R&D Associates Suite 500 1401 Wilson Blvd. Arlington, VA 22209 Attn: P. J. Turchi	1 copy
Mission Research Corporation 1400 San Mateo Blvd. SE Albuquerque, NM 87108 Attn: B. B. Godfrey	1 copy	R&D Associates P.O. Box 9695 Marina Del Rey, CA 90291 Attn: C. MacDonald	1 copy
National Science Foundation Mail Stop 19 Washington, DC 20550 Attn: D. Berley	1 copy	SAI 8400 W. Park Ave. McLean, VA 22102 Attn: A. Drobot	1 copy
Naval Research Laboratory Addressee: Attn: Name/Code Code 2628 - TID Distribution Code 1001 - T. Coffey Code 4000 - W. Ellis Code 4040 - J. Boris Code 4700 - S. L. Ossakow Code 4701 - I. M. Vitkovitsky Code 4710 - C. Kapetanakis Code 4720 - J. Davis Code 4730 - S. Bodner Code 4740 - W. Manheimer Code 4760 - B. Robson Code 4770 - G. Cooperstein Code 4770.1 - F. C. Young Code 4770.2 - R. Comisso Code 4771 - P. Ottinger Code 4771 - J. Grossmann Code 4771 - J. Neri Code 4773 - S. J. Stephanakis Code 4773 - R. A. Meger Code 4790 - D. Colombant Code 4790 - I. Haber Code 4790 - M. Lampe Code 6682 - D. Nagel Code 1220 Records	22 copies 1 copy 1 copy 1 copy 26 copies 1 copy 1 copy 5 copy 1 copy 1 copy 1 copy 10 copies 1 copy 1 copy 251 copies 1 copy 1 copy 1 copy 1 copy 1 copy 1 copy 1 copy 1 copy 1 copy 1 copy	Sandia National Laboratories P.O. Box 5800 Albuquerque, NM 87185 Attn: T. Martin/1250 J. P. Vandevender/1200 D. L. Cook/1260  Spire Corporation P.O. Box D Bedford, MA 01730 Attn: R. G. Little  Stanford University SLAC P.O. Box 4349 Stanford, CA 94305 Attn: W. B. Herrmannsfeldt  University of California Irvine, CA 92717 Attn: N. Rostoker  University of Washington Dept. of Nuclear Engineering BF-10 Seattle, WA 98115 Attn: F. Ribe	1 copy 1 copy 1 copy 1 copy  1 copy       1 copy       1 copy
Physics International Co. 2700 Merced Street San Leandro, CA 94577 Attn: C. Stallings	1 copy	U.S. Department of Energy Division of Inertial Fusion Washington, DC 20545 Attn: L. E. Killion M. Sluyter R. L. Schriever	1 copy 1 copy 1 copy
Pulse Sciences, Inc. 1615 Broadway, Suite 610 Oakland, CA 94612 Attn: S. Putnam	1 copy	U.S. Department of Energy P.O. Box 62 Oak Ridge, TN 37830  Director of Research U.S. Naval Academy Annapolis, MD 21402	1 copy   2 copies

END

DTIC

7-86